

## Simple extension of the plane-wave final state in photoemission: Bringing understanding to the photon-energy dependence of two-dimensional materials

Christian S. Kern<sup>1</sup>, Anja Haags<sup>2,3,4</sup>, Larissa Egger<sup>1</sup>, Xiaosheng Yang<sup>2,3,4</sup>, Hans Kirschner<sup>5</sup>, Susanne Wolff<sup>6,7</sup>, Thomas Seyller<sup>6,7</sup>, Alexander Gottwald<sup>5</sup>, Mathias Richter<sup>5</sup>, Umberto De Giovannini<sup>8,9</sup>, Angel Rubio<sup>8,10</sup>, Michael G. Ramsey<sup>1</sup>, François C. Bocquet<sup>2,3</sup>, Serguei Soubatch<sup>2,3</sup>, F. Stefan Tautz<sup>2,3,4,\*</sup>, Peter Puschnig<sup>1,†</sup> and Simon Moser<sup>11,‡</sup>

<sup>1</sup>Institute of Physics, NAWI Graz, University of Graz, 8010 Graz, Austria

<sup>2</sup>Peter Grünberg Institut (PGI-3), Forschungszentrum Jülich, 52425 Jülich, Germany

<sup>3</sup>Jülich Aachen Research Alliance (JARA), Fundamentals of Future Information Technology, 52425 Jülich, Germany

<sup>4</sup>Experimental Physics IV A, RWTH Aachen University, 52074 Aachen, Germany

<sup>5</sup>Physikalisch-Technische Bundesanstalt (PTB), 10587 Berlin, Germany

<sup>6</sup>Institute of Physics, Chemnitz University of Technology, 09107 Chemnitz, Germany

<sup>7</sup>Center for Materials, Architectures and Integration of Nanomembranes (MAIN), Chemnitz University of Technology, 09107 Chemnitz, Germany

<sup>8</sup>Max Planck Institute for the Structure and Dynamics of Matter, 22761 Hamburg, Germany

<sup>9</sup>Dipartimento di Fisica e Chimica-Emilio Segrè, Università degli Studi di Palermo, 90123 Palermo, Italy

<sup>10</sup>Center for Computational Quantum Physics (CCQ), Flatiron Institute, New York, New York 10010, USA

<sup>11</sup>Physikalisches Institut and Würzburg-Dresden Cluster of Excellence ct.qmat, Universität Würzburg, 97074 Würzburg, Germany



(Received 25 April 2023; accepted 23 June 2023; published 3 August 2023)

Angle-resolved photoemission spectroscopy (ARPES) is a method that measures orbital and band structure contrast through the momentum distribution of photoelectrons. Its simplest interpretation is obtained in the plane-wave approximation, according to which photoelectrons propagate freely to the detector. The photoelectron momentum distribution is then essentially given by the Fourier transform of the real-space orbital. While the plane-wave approximation is remarkably successful in describing the momentum distributions of aromatic compounds, it generally fails to capture kinetic-energy-dependent final-state interference and dichroism effects. Focusing our present study on quasi-freestanding monolayer graphene as the archetypical two-dimensional (2D) material, we observe an exemplary  $E_{\text{kin}}$ -dependent modulation of, and a redistribution of spectral weight within, its characteristic *horseshoe* signature around the  $\bar{K}$  and  $\bar{K}'$  points: both effects indeed cannot be rationalized by the plane-wave final state. Our data are, however, in remarkable agreement with *ab initio* time-dependent density functional simulations of a freestanding graphene layer and can be explained by a simple extension of the plane-wave final state, permitting the two dipole-allowed partial waves emitted from the C  $2p_z$  orbitals to scatter in the potential of their immediate surroundings. Exploiting the absolute photon flux calibration of the Metrology Light Source, this scattered-wave approximation allows us to extract  $E_{\text{kin}}$ -dependent amplitudes and phases of both partial waves directly from photoemission data. The scattered-wave approximation thus represents a powerful yet intuitive refinement of the plane-wave final state in photoemission of 2D materials and beyond.

DOI: [10.1103/PhysRevResearch.5.033075](https://doi.org/10.1103/PhysRevResearch.5.033075)

### I. INTRODUCTION

Angle-resolved photoemission spectroscopy (ARPES) is a standard probe of the surface electronic structure of crystalline solids. Within the one-step model, the differential photoemission cross section  $d\sigma/d\Omega(k_f, \Omega_{k_f}; h\nu, \epsilon)$ , i.e., the probability density to observe after irradiation with photons of energy  $h\nu$

and polarization vector  $\epsilon$  a photoelectron of kinetic energy  $E_{\text{kin}} = \hbar^2 k_f^2 / 2m$  and wave vector  $\mathbf{k}_f$  at solid angle  $\Omega_{k_f} = (\theta, \phi)$ , where  $\theta$  is the inclination and  $\phi$  the azimuth, can be decomposed into a product of two terms [1,2]: the one-electron removal spectral function and the photoemission matrix element  $M_{\mathbf{k}_f,i}$ . Usually, the spectral function is of primary interest because it provides access to band dispersions as well as self-energies and many-body interactions [2,3]. Often, however, the photoemission cross section is strongly modulated by the matrix element  $M_{\mathbf{k}_f,i}$ , given in the dipole approximation and velocity gauge by

$$M_{\mathbf{k}_f,i} = \langle \psi_{\mathbf{k}_f} | \epsilon \cdot \nabla | \psi_i \rangle, \quad (1)$$

through the latter's dependence on the single-particle initial ( $\psi_i$ ) and final state ( $\psi_{\mathbf{k}_f}$ ) wave functions, as well as on the polarization  $\epsilon$  of the incoming photon field. On the one hand,

\*s.tautz@fz-juelich.de

†peter.puschnig@uni-graz.at

‡simon.moser@physik.uni-wuerzburg.de

Published by the American Physical Society under the terms of the Creative Commons Attribution 4.0 International license. Further distribution of this work must maintain attribution to the author(s) and the published article's title, journal citation, and DOI.

this makes the experimental determination of the spectral function more difficult; on the other hand, the matrix element itself is a rich source of additional experimental information—especially regarding the initial-state wave function [4,5].

A particularly simple connection with the initial state follows when approximating the final state by a plane wave [6,7]. Then the matrix element becomes proportional to the Fourier transform of the initial state times a momentum-dependent prefactor:  $\epsilon \cdot \mathbf{k}_f \times \mathcal{F}[\psi_i](\mathbf{k}_f)$ . In the field of organic molecular films, this plane-wave approximation (PWA) turned out to be particularly fruitful, and the ability to determine molecular orbital densities in momentum and real space from ARPES on such films—becoming known as photoemission orbital tomography [5,8,9]—has found widespread applications [4,10–17]. Moreover, the PWA has also been applied to extended solid-state systems [5,18] and has provided insights into orbital angular momentum [19–21] and its topological manifestation in the Berry curvature [22–24].

Yet one can rightly argue that the relationship between the initial state and the matrix element is in fact more complex than the PWA suggests [25]. Examples where the limitations of the PWA become evident are manifold and include photoelectron diffraction [26,27], linear and circular dichroism [5,21,28], and photon-energy-dependent photoemission intensity modulations that have been tentatively attributed to final-state scattering effects [29,30]. Theoretically, there is a long history of computational approaches aiming at a more exact description of the photoemission process. These include sophisticated quantum-coherent one-step models such as implemented, e.g., in the spin-polarized relativistic Korringa-Kohn-Rostoker technique [31–33] and multiple-scattering approaches [27,30,34,35], but also real-time simulations in the framework of time-dependent density functional theory (TDDFT) [36,37]. While all these methods adequately capture the photoemission process on a microscopic level, they hide the underlying physical mechanisms in the computational complexity, thus rendering it impractical to establish any simple and intuitive connection between the matrix element and the initial state. Still, such a connection is vital for the physical understanding of photoemission, in particular in the context of orbital tomography.

In this paper we present an economical extension of the plane-wave final state in photoemission from two-dimensional (2D) materials that takes into account all essential physical effects while retaining an intuitive link to the initial state. We used the photoemission intensity close to the  $\bar{K}$  point of quasi-freestanding monolayer graphene (QFMLG) [38–40], prepared on Si-terminated 6H-SiC(0001), as a benchmarking case (see Appendix A for details of sample preparation). Varying the photon energy  $h\nu$  in small steps, we measured the influence of the corresponding final state on the differential photoemission cross section of a constant initial state within the Dirac bands. We found that real-time TDDFT calculations employing the surface-flux method [37] corroborate our benchmarking experiment. Crucially, we then introduce an intuitive *scattered-wave approximation* (SWA) of the photoemission final state that involves the interference of two dipole-allowed partial waves emitted from each C  $2p_z$  orbital and optionally their nearest-neighbor scattering at both sublattices of graphene as well (SWA<sup>NN</sup>). This final-

state model describes the experimental results and the TDDFT calculations very well. Because of its generic nature, it can be readily used for a graphene-based determination of the absolute photon flux for variable energies, arbitrary experimental geometries, and light polarizations typical for synchrotron-radiation experiments. Ultimately the model can be further adapted to other (quasi-) 2D materials, such as films of  $\pi$ -conjugated molecules or (topological) surface states, to correct for deficiencies of the PWA in the description of their circular dichroism and photon-energy dependence, properties that in turn massively influence the extraction of the quantum metric and the Berry curvature [22–24].

## II. RESULTS

In our ARPES experiment, we employ a toroidal electron analyzer to measure the photoelectron intensity distribution  $I(k_f, \Omega_0, \varphi; h\nu, \epsilon)$  at the detector, with  $\Omega_0 = (\theta, \phi = 0)$  and  $k_f = \sqrt{2mE_{\text{kin}}/\hbar^2} = \sqrt{2m(h\nu + \epsilon_i - \Phi)/\hbar^2}$ , where  $\Phi$  is the work function, and where  $\varphi$  is the azimuthal rotation of the sample (see Appendix B for details). The index  $f$  denotes the final state, as defined by the fixed initial-state energy  $\epsilon_i$  1.35 eV below the Dirac point, and by the varying photon energy  $h\nu$ . Apart from an efficiency factor of the analyzer,  $I$  is proportional to the differential photoemission cross section  $d\sigma/d\Omega(k_f, \Omega_0, \varphi; h\nu, \epsilon)$  and the photon intensity  $I_{\text{ph}}(h\nu, \epsilon)$  (see Appendix C for details). Recovering  $d\sigma/d\Omega$  from the photoelectron intensity distribution thus requires a division by an absolutely calibrated  $I_{\text{ph}}$ , which was readily provided by the insertion device beam line at the Metrology Light Source in Berlin [41] for photon energies from 15 to 110 eV (see Appendix B for details). Converting  $(\theta, \varphi)$  to  $(k_x, k_y)$  and plotting the corresponding measured *momentum maps* in Figs. 1(a) and 1(b), we identify graphene's characteristic *horseshoe signatures* around the  $\bar{K}$  and  $\bar{K}'$  points [42,43]. They arise from the structural interference of the two sublattices in the initial-state Bloch wave function and are thus characteristic for the honeycomb lattice. Specifically, the lattice sites' relative geometric phases  $\vartheta_{\mathbf{k}} = \arg \sum_{j=0}^2 e^{i\mathbf{n}_j \cdot \mathbf{k}}$  [Figs. 1(c) and 2(a)], where the  $\mathbf{n}_j$  connect neighboring carbon atoms, produce a structure factor  $(1 + e^{i\vartheta_{\mathbf{k}}})$  that suppresses valence band intensity along *dark corridors* [43] in momentum space [Fig. 1(a) and Appendix D]. While in the PWA, both horseshoe and dark corridor are not expected to change, the experimental intensity around the horseshoes clearly redistributes as a function of final-state kinetic energy [43], as illustrated in Fig. 1(e). Importantly, similar intensity redistributions as in experiment are also observed in our TDDFT simulations [Fig. 1(e); see Appendix E for details], suggesting their source to be found in the final state.

To aid the quantitative analysis of the momentum maps, we plotted the photoelectron intensity as a function of the angle  $\beta$  around the green contour in Fig. 1(b) for  $E_{\text{kin}}$  between 15 and 80 eV [leftmost column of Figs. 2(c)–2(e)], in normal light incidence [NI, Fig. 2(a)] and oblique light incidence [OI, Fig. 2(b)] geometries, both with  $p$  polarization. In NI geometry [Fig. 2(c)], the intensity appears predominantly below  $E_{\text{kin}} \lesssim 50$  eV, contracted along two streaks at  $\beta \sim \pm\pi/3$  and interrupted by homogeneous intensity distributions between

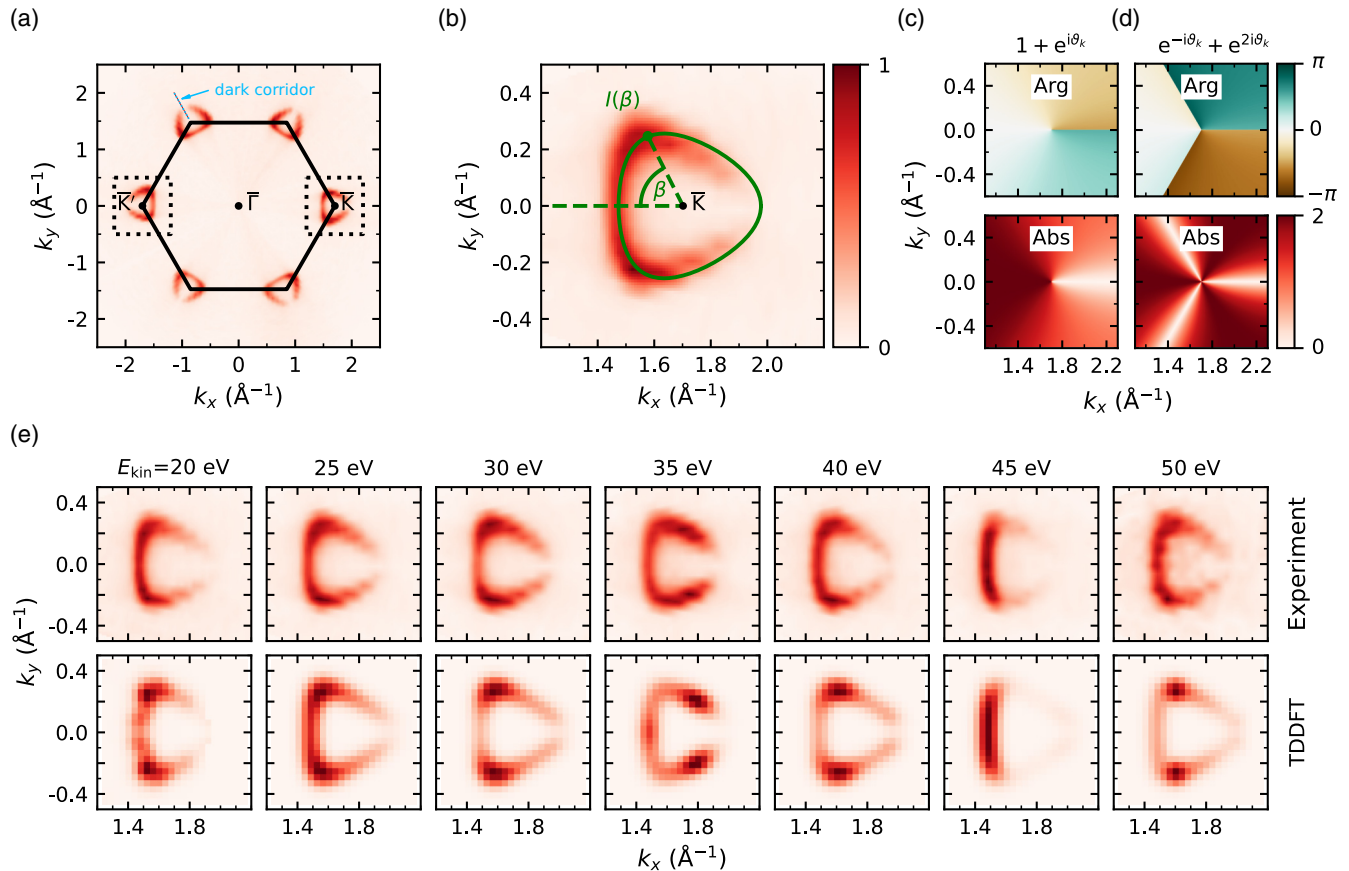


FIG. 1. Angle-resolved photoemission spectroscopy of graphene. Overview (a) and close-up (b) of the typical horseshoe pattern arising in momentum maps close to the  $\bar{K}$  and  $\bar{K}'$  points, recorded at initial-state energy 1.35 eV below the Dirac point at  $E_{\text{kin}} = 30$  eV. Panel (b) also displays the contour (green line) and angle  $\beta$  along which the experimental data are plotted in Figs. 2(c)–2(e). (c) Amplitude (bottom) and phase (top) of the initial-state structure factor that gives rise to the horseshoe. (d) Nearest-neighbor scattering factor that gives rise to intensity redistributions around the horseshoe. (e) Experimental horseshoe patterns around  $\bar{K}$  for seven representative kinetic energies measured in normal incidence geometry (top), compared to TDDFT calculations in precisely the same geometry (bottom).

these angles at  $\sim 44$  eV and below 20 eV. Further, between 30 and 40 eV we find the intensity to shift towards higher angles  $\beta = \pm 2\pi/3$ , an effect that we attribute to nearest-neighbor final-state scattering, as shall be seen in the following. In contrast, the angular intensity distribution in the OI geometry [Figs. 2(d) and 2(e)] is spread out more evenly between  $\beta = \pm\pi/3$ , because in this geometry nearest-neighbor scattering turns out to be less prevalent (see below). Moreover, the intensity distribution reaches up to kinetic energies of about 60 eV, with a suppression around 44 eV in the backward emission direction [BWD, Fig. 2(d)] that is not observed in forward emission [FWD, Fig. 2(e)].

As mentioned above, the PWA [second column in Figs. 2(c)–2(e)] does not reproduce the rich structure observed in experiment: it predicts a monotonous decay of intensity with increasing kinetic energy, without any redistribution around the horseshoe. Also, the polarization factor  $|\epsilon \cdot \mathbf{k}_f|^2$  of the PWA incorrectly suppresses the overall intensity in the OI BWD geometry, in which the photoemission occurs (nearly) perpendicular to the polarization vector of light [Figs. 2(b) and 2(d)]. In contrast, our TDDFT results [third column in Figs. 2(c)–2(e)] are in remarkable agreement with the experiment in all three geometries, apart from an

overall  $\sim 3$  eV kinetic energy shift with respect to the experiment. Because the TDDFT simulations were performed for a freestanding and perfectly flat graphene layer, the pronounced structure must originate from graphene itself, and thus alternative explanations for the experimentally observed features in the photoemission cross section, such as hybridization with the substrate, photoelectron scattering from the underlying substrate atoms, or buckling of the graphene layer, can be ruled out. As TDDFT, however, accurately models graphene's surface potential, it also fully accounts for scattering of the outgoing photoelectron in the graphene lattice itself, apart from an overall offset of the surface potential because of the missing SiC substrate, to which we attribute the above-mentioned overall kinetic energy shift.

To clarify the physical origin of the kinetic energy and wave vector dependence of the differential cross section, we developed an improved model for the final state, the scattered-wave approximation (SWA). In this model, scattering effects are included via angular-momentum-dependent and kinetic-energy-dependent amplitudes and phase shifts between partial waves of the outgoing Coulomb wave (see Appendix F and Ref. [21]). As a result,  $k_f$ -dependent interference effects in the final state between the two dipole-allowed  $l \pm 1$  partial

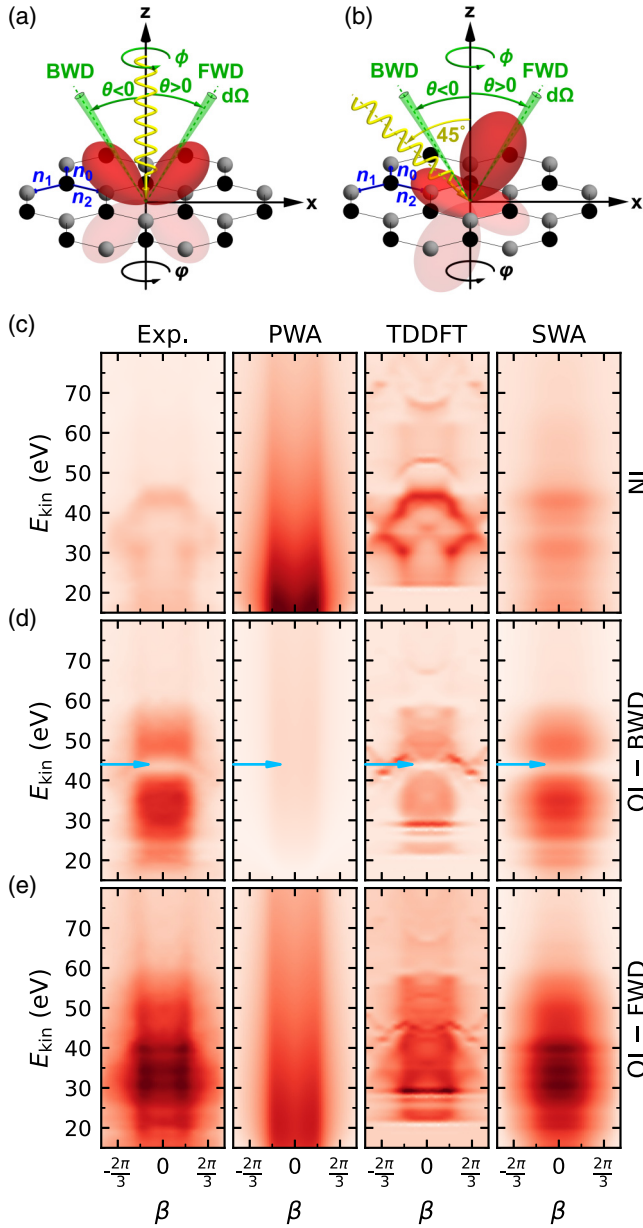


FIG. 2. Kinetic-energy-dependent photoemission intensities around the horseshoe. (a) Normal incidence (NI) geometry. (b) Oblique incidence (OI) geometry. The incident light polarization is shown by the yellow sine wave. Angle-resolved detection in  $d\Omega$  around inclination  $\theta$  and azimuth  $\phi$  is illustrated in green. The red lobes visualize the angular distributions of the pure  $d$  channels,  $d_{\text{NI}}^2$  and  $d_{\text{OI}}^2$ , respectively [cf. Eqs. (4) and (5)]. In our experiment only photoelectrons emitted into the  $(x, z)$  plane, where  $\phi = 0$ , are detected. To obtain the momentum maps in Fig. 1, the sample is rotated around the  $z$  axis by varying  $\phi$ . (c)–(e) Experimental photoemission intensities in three geometries as indicated, extracted along the green contour in Fig. 1(b) and compiled for densely sampled kinetic energies between 15 and 80 eV (first column), compared to predictions of the PWA (second column), TDDFT (third column, shifted by 3 eV), and SWA without nearest-neighbor scattering (fourth column). Intensities in each column are plotted to scale, with dark red corresponding to high intensity. Between the columns the scaling is arbitrary. The blue arrows mark an intensity minimum that arises from a node in the  $d$  channel.

waves become possible. While this description has in fact a long history in the simulation of the photoemission process of gas-phase molecules [44–47], we formally extended it to a periodic system, including the Bloch nature of the initial state as well as on-site, and, in a second step, nearest-neighbor scattering of the outgoing photoelectron.

Without nearest-neighbor scattering, the photoemission intensity from the C  $2p_z$ -derived valence band of graphene becomes (see Appendix F)

$$I(k_f, \Omega_{k_f}, h\nu, \epsilon) \propto |M_{k_f, k}|^2 = \delta_{k, k_{f\parallel}} |\epsilon \cdot \mathbf{M}_{210}(k_f)(1 + e^{i\vartheta_k})|^2, \quad (2)$$

where the Kronecker  $\delta_{k, k_{f\parallel}}$  describes momentum conservation (modulo reciprocal lattice translations) and  $(1 + e^{i\vartheta_k})$  is the initial-state structure factor. Remarkably, the term  $\epsilon \cdot \mathbf{M}_{nlm}(k_f)$  now replaces  $\epsilon \cdot \mathbf{k}_f \times \mathcal{F}[\phi_{nlm}](k_f)$  in the PWA that we discussed in the introduction. For a  $2p_z$  orbital with quantum numbers  $\{nlm\} = \{210\}$ , it is given by

$$\mathbf{M}_{210}(k_f) = \underbrace{\tilde{g}(k_f) \mathbf{Y}_{1,0,0}(\theta, \phi)}_{s \text{ channel}} - \underbrace{\tilde{f}(k_f) \mathbf{Y}_{1,2,0}(\theta, \phi)}_{d \text{ channel}} \quad (3)$$

and therefore embodies the dipole selection rule and the corresponding angular distribution in the differential cross section for photoemission from C  $2p_z$  orbitals. The complex-valued quantities  $\tilde{g}(k_f)$  and  $\tilde{f}(k_f)$  are determined by the effective on-site scattering potential and contain the  $k_f$ -dependent amplitude and phase of the  $s$  and  $d$  photoemission partial waves, respectively. The photoemission angular distribution in these two channels is given by the vector spherical harmonics  $\mathbf{Y}_{l,l\neq 1,m}$  [48], whose components can be individually addressed by the principal components of the light polarization vector  $\epsilon$ .

In our experimental geometry [Figs. 2(a) and 2(b)], the NI and OI intensities simplify to (see Appendix F)

$$I_{\text{NI}} \propto |\tilde{f}(k_f)|^2 d_{\text{NI}}(\theta, \phi)^2 |1 + e^{i\vartheta_{k_{f\parallel}}}|^2, \quad (4)$$

$$I_{\text{OI}} \propto [|\tilde{f}(k_f)|^2 d_{\text{OI}}(\theta, \phi)^2 + 8|\tilde{g}(k_f)|^2 + 4\sqrt{2}|\tilde{f}(k_f)||\tilde{g}(k_f)|d_{\text{OI}}(\theta, \phi)\cos\Delta\sigma]|1 + e^{i\vartheta_{k_{f\parallel}}}|^2, \quad (5)$$

where  $d_{\text{NI}}(\theta, \phi) = \sin 2\theta \cos \phi$  and  $d_{\text{OI}}(\theta, \phi) = 3 \sin 2\theta \cos \phi + 3 \cos 2\theta + 1$  describe the angular intensity distributions of the pure  $d$  channel in the respective polarization geometries, and where  $\Delta\sigma = \arg(\tilde{f}/\tilde{g})$  describes the relative phase between  $s$  and  $d$  partial waves. In the symmetric NI geometry, the  $s$  channel is suppressed and emission in the  $d$  channel is symmetric in  $\theta$ . In contrast,  $I_{\text{OI}}$  is determined by the interference between the isotropic  $s$  and the anisotropic  $d$  channels. We note that in our experiments the plane of light incidence (spanned by the wave vector and light polarization) and the plane of detected photoemission coincide, i.e.,  $\phi = 0$ . Hence, for  $\beta = 0$  the above equations apply directly to our experiment, while for  $\beta \neq 0$  [equivalent to  $\phi \neq 0$  in Figs. 2(a) and 2(b) and Eq. (4)] the sample and with it the initial state need to be rotated by changing  $\phi$  away from 0 while keeping  $\phi = 0$ . In contrast, both the TDDFT and the SWA calculations in Figs. 2(c)–2(e) vary  $\phi$  and keep  $\phi = 0$ . Because the variations

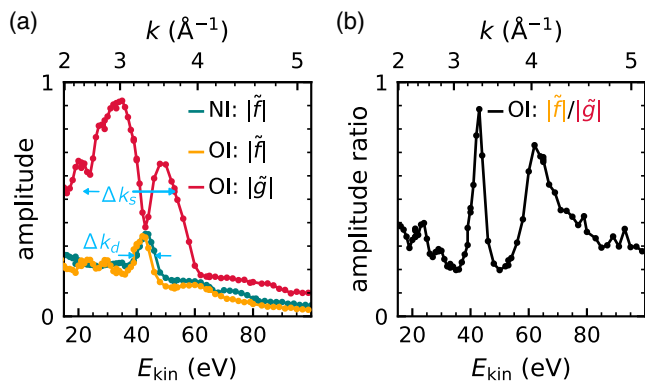


FIG. 3. Photoemission into  $s$  and  $d$  channels as a function of final-state kinetic energy. (a) Amplitudes  $|\tilde{g}|$  and  $|\tilde{f}|$  of the  $s$  and  $d$  channels, respectively; (b) their ratio in the OI geometry. The curves were extracted from experimental data at  $\beta = 0$  in NI and OI geometries as indicated, using the SWA without nearest-neighbor scattering. Positive real values were obtained only for in-phase photoemission in the  $s$  and  $d$  channels, i.e.,  $\Delta\sigma = 0$ .

of  $\varphi$  (experiments) and  $\phi$  (calculations) along the horseshoe trajectory  $\beta$  are small, deviations between the two detection geometries are negligible, as is also illustrated by the excellent agreement between experiment and theory in Figs. 2(c)–2(e).

In analyzing the predictions of the SWA, we first focus on the kinetic energy ( $k_f$ ) dependence. Since  $d_{\text{OI}}(\phi = 0, \theta)^2$  vanishes for backward emission at  $\theta_0^- \approx -29.3^\circ$ , we expect a minimum in  $I_{\text{OI}}$  at this angle. Close to the  $\bar{K}$  point of graphene we have  $k_{\parallel} \approx 1.7 \text{ \AA}^{-1}$ . Photoelectrons with this  $k_{f\parallel}$  will be emitted at the angle  $\theta_0^-$  if  $k_f = k_{f\parallel} / \sin \theta_0^-$ , yielding a kinetic energy  $E_{\text{kin}} \approx 44 \text{ eV}$ . This agrees with the observed intensity minimum in backward emission displayed in Fig. 2(d) (blue arrows), which can therefore be assigned to a node in the  $d$  channel [red lobe in Fig. 2(b)]. Note that the second root of  $d_{\text{OI}}(\phi = 0, \theta)^2$  appears in forward direction at  $\theta_0^+ \approx 74.3^\circ$ , corresponding to a kinetic energy of only 11.4 eV for electrons from the vicinity of the  $\bar{K}$  point, which is outside our measurement range.

With the help of Eqs. (4) and (5) it is in fact possible to reconstruct the functions  $|\tilde{g}(k_f)|$  and  $|\tilde{f}(k_f)|$ . To this end, we divided the NI experimental data in Fig. 2(c) at fixed angle  $\beta = 0$  by  $\sin^2 2\theta$  and thereby extracted the amplitude  $|\tilde{f}(k_f)|$  of the  $d$  channel (at  $\beta = 0$ , we also have  $\phi = 0$ ). The green curve in Fig. 3(a) displays the result. Similarly, the BWD and FWD OI geometries [Figs. 2(d) and 2(e)] at  $\beta = 0$  deliver two linearly independent equations for  $I_{\text{OI}}(k_f)$ . Solving these for  $|\tilde{f}(k_f)|$  [orange in Fig. 3(a)] and  $|\tilde{g}(k_f)|$  [red in Fig. 3(a)], we find positive real values only if  $\Delta\sigma = 0$ , i.e., for an in-phase emission in the  $s$  and  $d$  channels. Quite remarkably,  $|\tilde{f}(k_f)|$  obtained from the OI geometry matches the curve obtained from the NI geometry absolutely, i.e., without any scaling correction, thereby underlining the excellent photon intensity calibration provided by the Metrology Light Source. Plotting the ratio  $|\tilde{f}|/|\tilde{g}|$  in Fig. 3(b), we find the  $s$  channel to be the predominant photoelectron source throughout the entire energy regime, except for regions around 43 eV and 63 eV, where the  $s$  and  $d$  channel contributions are of the same order.

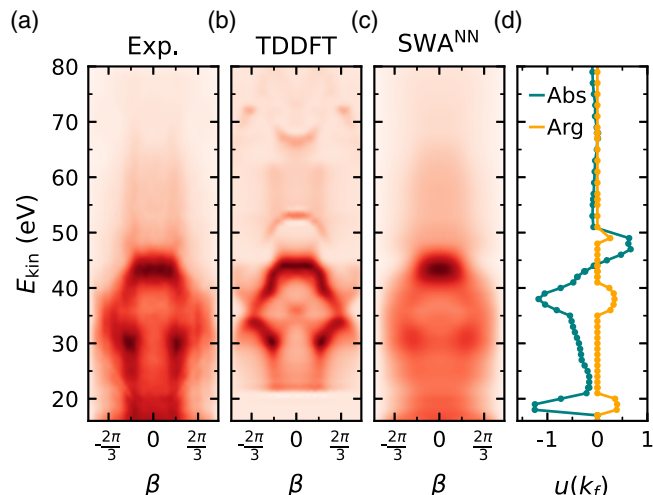


FIG. 4. Influence of nearest-neighbor scattering. (a) Experimental photoemission intensity in the NI geometry reproduced from Fig. 2(c) with a different contrast scaling. (b) Corresponding TDDFT simulations from Fig. 2(c). (c) SWA<sup>NN</sup> prediction including nearest-neighbor final-state scattering. (d)  $k_f$ -dependent scattering amplitude and phase of  $u(k_f)$  that best fit the data in (a). For a compact display we have plotted  $\text{Abs} \equiv |u| \times \text{sgn}(\arg u)$  and  $\text{Arg} \equiv \text{mod}(\arg u, \pi)$ .

Inserting the so-obtained amplitudes  $|\tilde{f}(k_f)|$  and  $|\tilde{g}(k_f)|$  as well as the phase shift  $\Delta\sigma = 0$  back into the model of Eq. (2), we can calculate the expected intensity distribution in the horseshoe for our three experimental configurations (varying  $\theta$  and  $\phi$  and keeping  $\varphi = 0$ ). The results are shown in the rightmost column of Figs. 2(c)–2(e). Regarding the OI data [Figs. 2(d) and 2(e),] which exhibit relatively little structure in  $\beta$ , the agreement between experiment and SWA is very satisfactory and clearly much better than for the PWA. For the NI data, however, the SWA model does not capture the distinctive redistribution of the intensity in  $k$ -space that is observed in experiment. Specifically, the kinetic-energy-dependent modulation along  $\beta$  is not reproduced.

To amend this deficiency, we thus extended the model to include, in addition to on-site scattering, also nearest-neighbor (NN) scattering in the final state, i.e., scattering of photoelectrons emitted from sublattice A into the Coulomb partial waves centered at one of the neighboring B sites. Adapting Eq. (2) accordingly, we find (see Appendix F)

$$I(k_f, \Omega_{k_f}, h\nu, \epsilon) \propto |\epsilon \cdot \mathbf{M}_{210}(\mathbf{k}_f)| \times [1 + e^{i\vartheta_k} + (e^{-i\vartheta_{k_{f\parallel}}} + e^{i\vartheta_k} e^{i\vartheta_{k_{f\parallel}}})u(\mathbf{k}_f)]^2 \delta_{\mathbf{k}, \mathbf{k}_{f\parallel}}. \quad (6)$$

NN final-state scattering thus leads to an additional term  $(e^{-i\vartheta_{k_{f\parallel}}} + e^{i\vartheta_k} e^{i\vartheta_{k_{f\parallel}}})u(\mathbf{k}_f)$ , which collapses to  $(e^{-i\vartheta_{k_{f\parallel}}} + e^{i2\vartheta_{k_{f\parallel}}})u(\mathbf{k}_f)$  due to momentum conservation. Because  $u(\mathbf{k}_f)$  varies only slowly on the photoemission hemisphere  $\Omega_{k_f}$ , for a given  $k_f$  it can be approximated in Eq. (6) as a merely kinetic-energy-dependent (but not momentum-vector-dependent) fit parameter  $u(k_f)$  that is constant around the horseshoe, i.e.,  $u(\mathbf{k}_f) \approx |u(k_f)|e^{i \arg u(k_f)}$ . Fitting Eq. (6) under this assumption to the experimental data of Fig. 2(c), we obtained the intensity distribution shown in Fig. 4(c), with the corresponding  $u(k_f)$

displayed in Fig. 4(d). Given the simplicity of our scattering model, the agreement with the experiment in Fig. 4(a) [and with TDDFT in Fig. 4(b)] is very satisfactory: In particular, the shift of the intensity to  $\beta \approx \pm 2\pi/3$  in the kinetic energy range between 30 and 40 eV and also below 20 eV, as well as the concurrent depletion of the intensity in the interval  $[-\pi/3, +\pi/3]$ , are well reproduced. As Fig. 1(d) reveals, these redistributions are a direct consequence of the minima and maxima of  $|e^{-i\vartheta_{k_f\parallel}} + e^{i2\vartheta_{k_f\parallel}}|$  at  $\beta = \pm\pi/3$  and  $\beta = \pm 2\pi/3$ , respectively, and the maxima of  $|u(k_f)|$  in the respective kinetic energy ranges. This demonstrates that the SWA in conjunction with nearest-neighbor final-state scattering (SWA<sup>NN</sup>) captures the essence of the observed intensity distribution, in both kinetic energy and  $k$ -space.

Looking back at the overall intensity distributions in  $\beta$  of the three experimental geometries in Figs. 2(c)–2(e), we note that nearest-neighbor final-state scattering is most prevalent in the NI geometry, to a much lesser extent also in the OI-FWD, but essentially absent in OI-BWD, where the intensity is essentially confined in the interval  $[-\pi/3, +\pi/3]$ , as predicted by the bare initial-state structure factor  $|1 + e^{i\vartheta_k}|$  [Fig. 1(c)]. In other words, experimental geometries that have significant  $d$  channel contributions [NI, OI-FWD, cf. Eqs. (4) and (5)] show NN scattering, while those with a dominant  $s$  channel (OI-BWD) do not. We rationalize this observation by the emission channels'  $k_f$  dependences. Estimating the  $d$  and  $s$  wave resonances in Fig. 3(a) to exhibit widths of  $\Delta k_d \approx 0.3 \text{ \AA}^{-1}$  and  $\Delta k_s \approx 1.5 \text{ \AA}^{-1}$ , respectively, Heisenberg's uncertainty principle  $\Delta k \Delta r \geq \hbar/2$  suggests real-space distributions of the corresponding Coulomb partial waves of the order  $\Delta r_d \approx 1.7 \text{ \AA}$  and  $\Delta r_s \approx 0.3 \text{ \AA}$  around the carbon nucleus. Taking into account a carbon-carbon distance of  $1.42 \text{ \AA}$ , a significant overlap between partial waves emanating from nearest neighbors is thus only expected for the  $d$  channel.

### III. CONCLUSION

In summary, we measured angle-resolved photoemission intensities of the horseshoe of quasi-freestanding monolayer graphene (QFMLG) for a wide range of photon energies using a calibrated photon flux. Varying the final-state kinetic energy for a fixed initial state, we found a complex intensity modulation that is well reproduced by simulations using the surface-flux method within the framework of TDDFT, but goes beyond the predictions of the plane-wave final state approximation. In order to understand these findings in terms of an intuitive physical picture, we developed the scattered-wave approximation for the photoemission final state, which allows for the interference of the dipole-allowed  $s$  and  $d$  photoemission channels, where the latter experiences also significant scattering from the neighboring carbon atoms. In this way, we extracted the kinetic-energy-dependent amplitude and phase of both  $s$  and  $d$  partial waves, which present a benchmark for *ab initio* theories that focus on a more sophisticated description of the photoemission process and are pivotal for the understanding of dichroism. Our wide-energy-range  $\tilde{f}(k_f)$ ,  $\tilde{g}(k_f)$  data provided in Fig. 3(a) (see Supplemental Material Ref. [49]) along with Eqs. (2) and (3) also allow for an easy calculation of the horseshoe intensities with arbitrary

polarized light. A prospective application thereof could be an absolute calibration of photon flux in any photoemission measurement with variable photon energy and geometry purely based on the photoemission response of the robust 2D material QFMLG. Going beyond graphene, our model further promises an intuitive description of complex kinetic-energy-dependent intensity modulations and dichroism in layers of  $\pi$  conjugated organic molecules, or even in (quasi-) 2D quantum materials with more complex orbital low-energy electronic structures, including strong spin orbit coupling.

### ACKNOWLEDGMENTS

We thank J. Riley (La Trobe University, Australia) for experimental support. Funding support came from the Deutsche Forschungsgemeinschaft (DFG, German Research Foundation) under Germany's Excellence Strategy through the Würzburg-Dresden Cluster of Excellence on Complexity and Topology in Quantum Matter ct.qmat (EXC 2147, Project ID 390858490), through the Collaborative Research Centers SFB 1170 ToCoTronics (Project ID 258499086) and SFB 1083 Structure and Dynamics of Internal Interfaces (Project ID 223848855), through the Research Unit FOR 5242 Proximity-induced Correlation Effects in low dimensional Structures (Project SE 1087-16/1), as well as through projects Po 2226/2-1 and Ri 804/8-1. Further, we gratefully acknowledge funding from the Austrian Science Fund (FWF) (Project I3731). The computational results have been achieved using the computing facilities of the University of Graz and the Vienna Scientific Cluster (VSC).

### APPENDIX A: SAMPLE PREPARATION

The preparation of quasi-freestanding monolayer graphene (QFMLG) was performed in two steps [38,50–52]: First, a Si-terminated 6H-SiC(0001) surface was thermally decomposed to create zero-layer graphene (ZLG). Subsequently, the ZLG is decoupled from the substrate by annealing at  $550 \text{ }^\circ\text{C}$  in hydrogen atmosphere (880 mbar) to obtain QFMLG. The quality of the QFMLG was controlled with low-energy electron diffraction (LEED) and x-ray photoemission spectroscopy (XPS) with Al  $K_\alpha$  radiation. After preparation, the sample was transferred through air to the synchrotron for ARPES experiments. Before the ARPES experiments, the sample was cleaned by outgassing in ultrahigh vacuum ( $<10^{-9}$  mbar) at  $350 \text{ }^\circ\text{C}$  for 30 min. ARPES experiments with 45 eV photon energy revealed band maps typical for  $p$ -doped graphene with the Fermi level 0.1 eV below the Dirac point [38].

### APPENDIX B: PHOTOEMISSION EXPERIMENTS

Photon-energy-dependent ARPES experiments were conducted at the calibrated insertion device beamline [41] of the Metrology Light Source at the Physikalisch-Technische Bundesanstalt (PTB), the German national metrology institute in Berlin. Measurements in two experimental geometries were carried out, labeled as normal incidence (NI) and oblique incidence (OI), with incidence angles of, respectively,  $0^\circ$  and

45° relative to the sample surface normal. In both geometries, the incident light was *p*-polarized.

The photon energy was varied in small steps (1 eV for  $h\nu < 50$  eV, 2 eV for  $h\nu > 50$  eV) from  $h\nu = 15$  to 110 eV. To this end, several different undulator/monochromator/filter settings of the beamline were employed: (1) In the photon energy range from 15 to 31 eV, the third undulator harmonic with normal incidence onto the grating monochromator was employed; (2) in the range from 25 to 45 eV, the third harmonic with grazing incidence in combination with a Mg filter was used; (3) from 45 to 60 eV, the sixth harmonic with grazing incidence in combination with an Al filter was employed; (4) for 60 to 71 eV, the tenth harmonic with grazing incidence in combination with an Al filter was used; (5) for 71 to 87 eV, the tenth harmonic with grazing incidence in combination with a Be filter was employed; (6) and finally, for 87 to 110 eV the same setting as in (5) but in wiggler operation mode was used. The filters served to suppress both parasitic light from higher grating orders and stray light from the monochromator, reducing the false-light contribution to below 1% of the total [41].

Special care was taken regarding the calibration of the photon intensity  $I_{\text{ph}}$ . To this end, we employed the drain current caused by photoemission at the beam-line mirror. This current was referenced to an absolutely calibrated semiconductor photodiode, yielding an  $h\nu$ -dependent photon intensity curve measured in photons per second and nanoampere mirror current [29]. During the photoemission experiments from graphene, the mirror current was constantly monitored, yielding the calibrated photon intensity  $I_{\text{ph}}(h\nu, \epsilon)$ , which was further used in Eq. (C8).

To detect the photoelectrons, a toroidal electron analyzer [53] was used. The instrument simultaneously collects photoelectrons emitted into a wide angular range of  $-85^\circ \leq \theta \leq 85^\circ$  within the plane of incidence, i.e., the plane spanned by the incident light beam and the sample normal [see Fig. 2(a)], and an energy dispersion range of  $\approx 1$  eV. Additionally rotating the sample  $360^\circ$  around its azimuth  $\varphi$  in steps of  $1^\circ$ , we obtained  $I(k_f, \Omega_0, \varphi; h\nu, \epsilon)$  with  $\Omega_0 \equiv (\theta, \phi = 0)$ , and thus a complete experimental data cube, which was transformed into experimental momentum maps of the photoemission intensity  $I(k_x, k_y)$ . Note that unlike momentum maps that would be obtained from the intensity  $I(k_f, \Omega_{k_f}; h\nu, \epsilon)$  by converting  $\Omega_{k_f} = (\theta, \phi)$  into  $(k_x, k_y)$ , the experimental momentum map in this paper was measured with constant azimuth  $\phi = 0$ . To obtain photoemission intensities deriving from the fixed initial-state energy of  $\epsilon_i = -1.25$  eV, i.e., 1.35 eV below the Dirac point, the kinetic energy  $E_{\text{kin}}$  at which photoelectrons were detected was varied with photon energy  $h\nu$  such that  $E_{\text{kin}} = h\nu - E_c$ .  $E_c$  was determined by comparing the experimentally measured diameter of the horseshoe to the TDDFT-calculated one. For  $E_c = 1.6$  eV, the experimentally measured horseshoes had the same diameter as the TDDFT-calculated horseshoes 1.35 eV below the Dirac point. While the absolute photoelectron-to-counts conversion rate of the toroidal electron analyzer is unknown, we expect the response  $\chi(k_f)$  to be linear and independent of  $k_f$ , i.e., of kinetic energy. The cross sections reported in this work are thus given apart from a constant factor  $\chi$ , i.e., only in relative terms, and were thus normalized arbitrarily in Fig. 3.

### APPENDIX C: PHOTOEMISSION DIFFERENTIAL CROSS SECTION

In the one-step model of photoemission, the probability per unit time (or transition rate)  $W_{i,k_f}$  that a photoelectron with wave vector  $k_f$  is emitted from the single-particle initial state  $i$  is given by Fermi's golden rule

$$\begin{aligned} W_{i,k_f} &= \frac{2\pi}{\hbar} \left| \langle \psi_{k_f} | \frac{e}{m} \mathbf{A} \cdot \hat{\mathbf{p}} | \psi_i \rangle \right|^2 \delta(\epsilon_i - \epsilon_{k_f} - \Phi + h\nu) \\ &= \frac{2\pi e^2 \hbar |A_0|^2}{m^2} |\langle \psi_{k_f} | \epsilon \cdot \nabla | \psi_i \rangle|^2 \delta(\epsilon_i - \epsilon_{k_f} - \Phi + h\nu), \end{aligned} \quad (\text{C1})$$

where  $|\psi_i\rangle$  is the initial (bound) state vector with energy  $\epsilon_i < 0$  and  $|\psi_{k_f}\rangle$  is the final (unbound) state vector with kinetic energy  $E_{\text{kin}} = \epsilon_{k_f}$ , and  $\Phi > 0$  is the work function.  $\mathbf{A}$  is the vector potential of the photon field,  $\epsilon$  its polarization vector,  $\hat{\mathbf{p}}$  the momentum operator of the (photo)electron, and  $e$  and  $m$  are the electron's charge and mass, respectively. The perturbing operator  $\mathbf{A} \cdot \hat{\mathbf{p}}$  arises from the minimal coupling principle by taking into account that the momentum operator commutes with the vector potential in the Coulomb gauge.

The probability per unit time  $P_{i,k_f}$  that a photoelectron with kinetic energy  $E_{\text{kin}} = \hbar^2 k_f^2 / 2m$  is emitted from initial state  $i$  into any direction  $\Omega_{k_f} = (\theta, \phi)$  can be calculated as

$$P_{i,k_f} = \frac{1}{v_{k_f}} \int_{|k'_f|=k_f} d^3 k'_f W_{i,k'_f}, \quad (\text{C2})$$

where  $v_{k_f} = (2\pi)^3/V$  is the  $k_f$ -space volume per  $k_f$  vector.  $V$  is the (illuminated) real-space volume of the sample, in which  $\int_V d^3 r \psi_{k_f}^* \psi_{k_f} = 1$ . Note that for a given initial state  $\psi_i$  with energy  $\epsilon_i$  and due to energy conservation enforced by the delta function in Eq. (C1), the integration in Eq. (C2) projects out the angular dependence at a fixed absolute value  $k_f$ , i.e., kinetic energy as described earlier [4]. Using Eq. (C1), this becomes

$$\begin{aligned} P_{i,k_f} &= \frac{V}{(2\pi)^2} \frac{e^2 \hbar |A_0|^2}{m^2} \int_{2\pi} d\Omega_{k'_f} \int k'_f{}^2 dk'_f |\langle \psi_{k'_f} | \epsilon \cdot \nabla | \psi_i \rangle|^2 \\ &\quad \times \delta(k'_f - k_f) \frac{1}{|s'(k_f)|} \\ &= \frac{V}{(2\pi)^2} \frac{e^2 |A_0|^2 k_f}{\hbar m} \int_{2\pi} d\Omega_{k_f} |\langle \psi_{k_f} | \epsilon \cdot \nabla | \psi_i \rangle|^2, \end{aligned} \quad (\text{C3})$$

where  $s(k'_f) \equiv \epsilon_i - \hbar k'_f{}^2 / 2m - \Phi + h\nu$ .

The total cross section  $\sigma_{i,k_f}$  of the photoemission process from initial state  $i$  is related to  $P_{i,k_f}$  by

$$\frac{\sigma_{i,k_f}}{A_\square} \equiv n_{i,k_f} = P_{i,k_f} \Delta t, \quad (\text{C4})$$

where  $A_\square$  is the illuminated area on the sample and  $n_{i,k_f}$  is the fraction of emitted photoelectrons per photon hitting the area  $A_\square$  in the time interval  $\Delta t$ . Evidently,  $A_\square$  is given by  $V_{\text{ph}}/(c\Delta t)$ , where  $V_{\text{ph}}$  is the volume in which the energy of the photon field amounts to  $h\nu$  and  $c$  the velocity of light. After differentiation with respect to the solid angle  $\Omega$  we thus find

for the differential cross section

$$\frac{d\sigma_{i,k_f}}{d\Omega} = \frac{V_{\text{ph}}}{c} \frac{dP_{i,k_f}}{d\Omega}. \quad (\text{C5})$$

Note that both  $\frac{d\sigma_{i,k_f}}{d\Omega}$  and  $\frac{dP_{i,k_f}}{d\Omega}$  are functions not only of  $k_f$  and  $\Omega_{k_f} = (\theta, \phi)$ , but also of photon energy  $h\nu$  (which—because of the delta function in Eq. (C1)—selects possible initial states  $i$  according to their  $\varepsilon_i$ ) and light polarization  $\epsilon$ . Hence, we write  $\frac{d\sigma}{d\Omega}(k_f, \Omega_{k_f}; h\nu, \epsilon)$  from now on.

The normalization of the light field to the energy of one photon in the volume  $V_{\text{ph}}$  fixes the amplitude  $A_0$  of the vector field to

$$|A_0|^2 = \frac{\hbar}{\pi V_{\text{ph}} \epsilon_0 \nu}. \quad (\text{C6})$$

According to Eqs. (C3) and (C5), this finally yields the differential photoemission cross section

$$\frac{d\sigma}{d\Omega}(k_f, \Omega_{k_f}; h\nu, \epsilon) = \frac{d\sigma_{i,k_f}}{d\Omega} = \frac{V}{4\pi^3} \frac{e^2 k_f}{cm\epsilon_0 \nu} |\langle \psi_{k_f} | \epsilon \cdot \nabla | \psi_i \rangle|^2. \quad (\text{C7})$$

In experiment, we measure the photoelectron intensity  $I(k_f, \Omega_{k_f}; h\nu, \epsilon)$  at the detector in a finite solid angle  $\Delta\Omega$ , originating from the area  $A_{\square}$  on the sample which contains  $N$  photoemitters. The calibrated beamline produces a known monochromatic photon flux  $F_{\text{ph}}(h\nu, \epsilon)$ , yielding a photon intensity  $I_{\text{ph}}(h\nu, \epsilon) = F(h\nu, \epsilon)A_{\square}$  on the area  $A_{\square}$ . Photoelectrons are detected with efficiency  $\chi(k_f)$ . Therefore, the photoelectron intensity is given by

$$I(k_f, \Omega_{k_f}; h\nu, \epsilon) = \chi(k_f) I_{\text{ph}}(h\nu, \epsilon) N \frac{\frac{d\sigma}{d\Omega}(k_f, \Omega_{k_f}; h\nu, \epsilon)}{A_{\square}} \Delta\Omega. \quad (\text{C8})$$

Thus, the intensity ratio  $I(k_f, \Omega_{k_f}; h\nu, \epsilon)/I_{\text{ph}}(h\nu, \epsilon)$ , if obtained at a carefully calibrated beamline with a carefully characterized linear response  $\chi(k_f)$  of the analyzer, is a direct measure of the differential photoemission cross section. If we assume that the volume density of the photoemitters in the sample is  $\varrho$ , we can replace the ratio  $N/A_{\square}$  in the above equation by  $\varrho d$ , where  $d$  is the effective sampling depth.

#### APPENDIX D: PHOTOEMISSION INITIAL STATE

The unit cell of graphene contains two carbon atoms, one in each of the two sublattices A and B. The respective atoms are located at  $\mathbf{R}_A = \frac{a}{2\sqrt{3}}(0, -1)^{\text{T}}$  and  $\mathbf{R}_B = \frac{a}{2\sqrt{3}}(0, 1)^{\text{T}}$  within the unit cell (see Fig. 5). Each of these carbon atoms contributes one  $2p_z$  orbital to the formation of aromatic  $\pi$  bonds. The nearest neighbors of carbon atoms in sublattice A are atoms in sublattice B; they are located at  $\mathbf{n}_0 = (0, a/\sqrt{3})^{\text{T}}$  within the same unit cell and at  $\mathbf{n}_1 = C_3^1 \mathbf{n}_0 = (-a/2, -a/2\sqrt{3})^{\text{T}}$  and  $\mathbf{n}_2 = C_3^2 \mathbf{n}_0 = (a/2, -a/2\sqrt{3})^{\text{T}}$  in adjacent unit cells, where  $C_3$  is a threefold rotation around the sample normal. In the orbital basis  $\{|R_A, 2p_z\rangle, |R_B, 2p_z\rangle\}$ , the tight-binding Hamiltonian with nearest-neighbor hopping reads

$$\hat{H} = t \begin{pmatrix} 0 & h(\mathbf{k}) \\ h^*(\mathbf{k}) & 0 \end{pmatrix}, \quad (\text{D1})$$

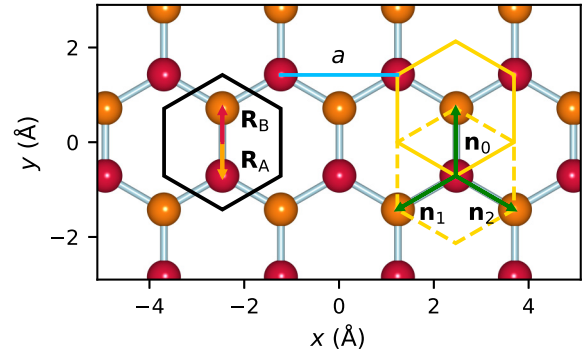


FIG. 5. Atomic structure of graphene. Carbon atoms of the two sublattices A and B are displayed in red and orange, respectively. The primitive unit cell containing one atom each of both sublattices is shown in black. The three vectors  $\mathbf{n}_0$ ,  $\mathbf{n}_1$ , and  $\mathbf{n}_2$  from an atom in sublattice A to its nearest neighbors in sublattice B are indicated in green. Nonprimitive unit cells that contain all nearest neighbors of a sublattice representative are shown in yellow. In the SWA<sup>NN</sup> including nearest-neighbor scattering, the total photoemission intensity is given by the sum of identical contributions from the two yellow unit cells.

where

$$h(\mathbf{k}) = \sum_{j=0}^2 e^{i\mathbf{n}_j \cdot \mathbf{k}} \equiv |h(\mathbf{k})| e^{i\vartheta_{\mathbf{k}}} \quad (\text{D2})$$

describes the coupling between sublattices A and B, and where  $t < 0$  is the nearest-neighbor hopping energy [54]. Diagonalizing  $\hat{H}$ , one finds eigenvalues

$$\begin{aligned} \varepsilon_{\mathbf{k}}^{\pm} &= \pm t |h(\mathbf{k})| \\ &= \pm t \sqrt{3 + 2 \cos(ak_x) + 4 \cos(ak_x/2) \cos(a\sqrt{3}k_y/2)} \end{aligned} \quad (\text{D3})$$

with eigenvectors  $\mathbf{c}^{\pm} = (c_A^{\pm}, c_B^{\pm})^{\text{T}} = \frac{1}{\sqrt{2}}(1, \pm e^{i\vartheta_{\mathbf{k}}})^{\text{T}}$ , where  $e^{i\vartheta_{\mathbf{k}}} = h(\mathbf{k})/|h(\mathbf{k})|$ , and where the superscripts + and – label the negative and positive energy solutions, i.e., the valence and the conduction band, respectively. The argument  $\vartheta_{\mathbf{k}}$  of  $h(\mathbf{k})$  is plotted in Fig. 6. Hence, the initial state of the photoemission process from the aromatic  $\pi$  bands of graphene is the Bloch state

$$\Psi_{\mathbf{k}}^{\pm}(\mathbf{r}) = \frac{1}{\sqrt{V}} \sum_{\mathbf{R}} e^{i\mathbf{k} \cdot \mathbf{R}} \frac{1}{\sqrt{2}} (|R_A, 2p_z\rangle \pm e^{i\vartheta_{\mathbf{k}}} |R_B, 2p_z\rangle), \quad (\text{D4})$$

where the sum runs over all graphene lattice sites  $\mathbf{R}$ , and  $\mathbf{k}$  is defined within the first Brillouin zone of graphene. Because in the experiment we measure only the horseshoe within the valence band of graphene, we exclusively select the + and drop the – solution.

#### APPENDIX E: TDDFT CALCULATIONS

For the *ab initio* simulations of photoemission from graphene, we restricted ourselves to a single layer with a carbon-carbon distance of  $n_j = 1.421$  Å, extended in the  $x$ ,  $y$  plane. The TDDFT simulations were carried out with the

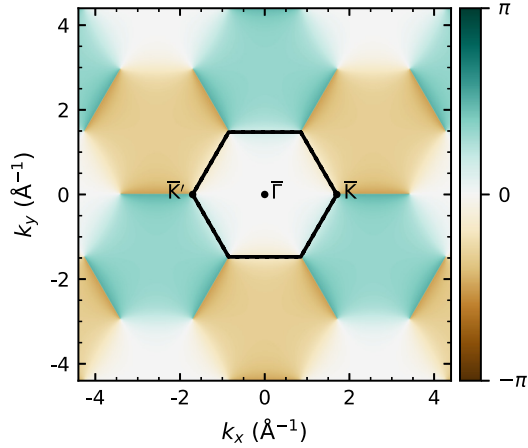


FIG. 6. Phase  $\vartheta_{\mathbf{k}}$  of graphene. The black hexagon indicates the first Brillouin zone.  $\bar{\Gamma}$ ,  $\bar{K}$ , and  $\bar{K}'$  points are labeled.

real-space real-time code OCTOPUS [55–57], using in-plane periodic boundary conditions and an out-of-plane simulation box of  $D_z = 70 \text{ \AA}$  in both directions. To avoid spurious reflections of electron density in both nonperiodic directions ( $\pm z$  directions), we inserted a complex absorbing potential [58] (CAP), starting at a distance of  $\pm 15 \text{ \AA}$  from the graphene layer, with  $i\xi \sin^2(\frac{\pi z}{2D_z})$  behavior and  $\xi = -1$  a.u. We used a grid spacing in the simulation box of  $0.18 \text{ \AA}$  and approximated the influence of the core electrons by norm-conserving Hartwigsen-Goedecker-Hutter pseudopotentials [59]. Exchange-correlation effects were treated in the adiabatic local density approximation (ALDA) [60,61].

After the electronic ground state had been calculated, the system was subjected to an electromagnetic field for 30 fs. It was coupled to the Hamiltonian in the velocity gauge. This pulse was modeled by a  $\cos(\omega t)$  function and shaped by a  $\sin^2$  hull function, thus ensuring gradual on- and off-switching. Over all times, we recorded the flux of electron density through a surface located at the onset of the CAP, which is a direct numerical simulation of the ARPES experiment [37,62]. In order to guarantee a normalized photon flux, the maximum amplitude of the pulse was varied for each photon energy, corresponding to a laser with a constant intensity of  $10^8 \text{ W/cm}^2$ .

## APPENDIX F: PHOTOEMISSION FINAL STATE

### 1. General framework

Following Ref. [21], we write the photoelectron final state in terms of unbound solutions of the Schrödinger equation in a central Coulomb potential (Coulomb wave equation), i.e., in terms of unbound (positive energy) hydrogen-like atomic orbitals  $|\mathbf{R}_j, \eta l m\rangle$  centered at site  $\mathbf{R}_j$ . These orbitals are the partial waves in the expansion of the Coulomb wave  $|\mathbf{k}_f\rangle$  with wave vector  $\mathbf{k}_f$  and as such are characterized by quantum numbers  $l$  and  $m$ , as well as the dimensionless Sommerfeld parameter  $\eta = Z/(a_0 k_f)$ , which describes the distortion of the outgoing photoelectron wave with spherical wave vector  $k_f$  in the Coulomb field of the ion that is left behind.  $a_0$  is the Bohr radius. Note that the Sommerfeld parameter takes the role

of the principal quantum number  $n$  that characterizes bound solutions.

The partial waves are given by [63–66]

$$\chi_{\eta l m}(\mathbf{r}) = \langle \mathbf{r} | \chi_{\eta l m} \rangle = R_{\eta l}(r) \langle \mathbf{r} | l m \rangle = R_{\eta l}(r) Y_l^m(\Omega_{\mathbf{r}}). \quad (\text{F1})$$

In the far field, the radial functions  $k_f r R_{\eta l}(r)$  normalize to a sine wave of unit amplitude,

$$R_{\eta l}(r \rightarrow \infty) \rightarrow \frac{\sin[k_f r - \eta \ln(2k_f r) - l\pi/2 + \sigma_l]}{k_f r}, \quad (\text{F2})$$

where  $\sigma_l = \arg \Gamma(l + 1 + i\eta)$  is the Coulomb phase. The sine wave is phase shifted with respect to the free electron wave, signifying the impact of the ionic Coulomb potential on the partial electron wave with angular momentum  $l$  far away from the atomic site.

The Coulomb wave  $|\mathbf{k}_f\rangle$  of the outgoing photoelectron emitted with wave vector  $\mathbf{k}_f$  from an atomic site in a specific direction, expanded in terms of partial waves for all  $l$  and  $m$ , is given by [67,68]

$$|\mathbf{k}_f\rangle = 4\pi \sum_{l=0}^{\infty} \sum_{m=-l}^l i^l e^{i\sigma_l} \langle l m | \mathbf{k}_f \rangle |\chi_{\eta l m}\rangle, \quad (\text{F3})$$

yielding

$$\begin{aligned} \chi_{\mathbf{k}_f}(\mathbf{r}) &= \langle \mathbf{r} | \mathbf{k}_f \rangle \\ &= 4\pi \sum_{l=0}^{\infty} \sum_{m=-l}^l i^l e^{i\sigma_l} R_{\eta l}(r, k_f) \langle \mathbf{r} | l m \rangle \langle l m | \mathbf{k}_f \rangle \\ &= 4\pi \sum_{l=0}^{\infty} \sum_{m=-l}^l i^l e^{i\sigma_l} R_{\eta l}(r, k_f) Y_l^m(\Omega_{\mathbf{r}}) Y_l^{m*}(\Omega_{\mathbf{k}_f}). \end{aligned} \quad (\text{F4})$$

This expression should be compared to the partial-wave expansion of the plane-wave final state

$$e^{i\mathbf{k}_f \cdot \mathbf{r}} = 4\pi \sum_{l=0}^{\infty} \sum_{m=-l}^l i^l j_l(k_f r) Y_l^{m*}(\Omega_{\mathbf{r}}) Y_l^m(\Omega_{\mathbf{k}_f}), \quad (\text{F5})$$

where the  $j_l$  are spherical Bessel functions.

The final-state wave function of a photoelectron with wave vector  $\mathbf{k}_f$  from a lattice of atoms is given by a coherent superposition of outgoing states  $|\mathbf{k}_f\rangle$  emanating from all sites,

$$\Psi_{\mathbf{k}_f}(\mathbf{r}) = \frac{1}{\sqrt{V}} \sum_{\mathbf{R}} e^{i\mathbf{k}_f \cdot \mathbf{R}} \sum_{\mathbf{R}_j} e^{i\mathbf{k}_f \cdot \mathbf{R}_j} \chi_{\mathbf{k}_f}(\mathbf{r} - \mathbf{R} - \mathbf{R}_j), \quad (\text{F6})$$

where the sums are carried out over all lattice vectors  $\mathbf{R}$  and basis sites  $\mathbf{R}_j$  within a unit cell of the lattice, respectively. The prefactor involving the normalization volume (=sample volume)  $V$  safeguards that  $\langle \Psi_{\mathbf{k}_f} | \Psi_{\mathbf{k}_f} \rangle = 1$ . In the case of graphene, this becomes

$$\Psi_{\mathbf{k}_f}(\mathbf{r}) = \frac{1}{\sqrt{V}} \sum_{\mathbf{R}} e^{i\mathbf{k}_f \cdot \mathbf{R}} \sum_{j=\{A,B\}} e^{i\mathbf{k}_f \cdot \mathbf{R}_j} \chi_{\mathbf{k}_f}(\mathbf{r} - \mathbf{R} - \mathbf{R}_j), \quad (\text{F7})$$

where all  $\mathbf{R}$ ,  $\mathbf{R}_j$  are 2D vectors in the plane of graphene.

Before turning to the special case of photoemission from the  $C 2 p_z$  orbitals of graphene, we derive a general expression for the matrix element in Eq. (C7) between an initial Bloch

state with band index  $\kappa$ ,

$$|\Psi_{\mathbf{k}}^{\kappa}\rangle = \frac{1}{\sqrt{V}} \sum_{\mathbf{R}} e^{i\mathbf{k}\cdot\mathbf{R}} \sum_{\mathbf{R}_j} \sum_{nlm} c_{jnlm}^{\kappa}(\mathbf{k}) |\mathbf{R} + \mathbf{R}_j, nlm\rangle, \quad (\text{F8})$$

and the final state as given in Eq. (F6). The initial-state Bloch state can be expanded in terms of atomic states with quantum numbers  $\{nlm\}$  centered at sites  $\mathbf{R} + \mathbf{R}_j$ . The latter are given by bound atomic orbitals (negative energy)

$$\Phi_{nlm}(\mathbf{r}) = \langle \mathbf{r} | \mathbf{0}, nlm \rangle = R_{nl}(r) Y_l^m(\Omega_r). \quad (\text{F9})$$

Note that for graphene, the Bloch wave vectors in Eq. (F8) are 2D and oriented in the surface plane, i.e.,  $\mathbf{k} = \mathbf{k}_{\parallel}$ . For the photoemission matrix element  $M_{k_f k}^{\kappa}$  between the initial-state wave function  $\Psi_{\mathbf{k}}^{\kappa}(\mathbf{r})$  and the final-state wave function  $\Psi_{k_f}(\mathbf{r})$  we obtain from Eq. (F6) and Eq. (F8)

$$\begin{aligned} M_{k_f k}^{\kappa} &= \int d^3r \Psi_{k_f}^*(\mathbf{r}) \boldsymbol{\epsilon} \cdot \nabla \Psi_{\mathbf{k}}^{\kappa}(\mathbf{r}) \\ &= \frac{1}{V} \sum_{\mathbf{R}'} e^{-i\mathbf{k}_f \cdot \mathbf{R}'} \sum_{\mathbf{R}_j'} e^{-i\mathbf{k}_f \cdot \mathbf{R}_j'} \sum_{\mathbf{R}} e^{i\mathbf{k} \cdot \mathbf{R}} \sum_{\mathbf{R}_j} \sum_{nlm} c_{jnlm}^{\kappa}(\mathbf{k}) \\ &\quad \times \int d^3r \chi_{k_f}^*(\mathbf{r} - \mathbf{R}' - \mathbf{R}_j') \boldsymbol{\epsilon} \cdot \nabla \Phi_{nlm}(\mathbf{r} - \mathbf{R} - \mathbf{R}_j) \\ &= \frac{1}{V} \sum_{\mathbf{R}'} e^{-i\mathbf{k}_f \cdot \mathbf{R}'} \sum_{\mathbf{R}_j'} e^{-i\mathbf{k}_f \cdot \mathbf{R}_j'} \sum_{\mathbf{R}} e^{i\mathbf{k} \cdot \mathbf{R}} \sum_{\mathbf{R}_j} \sum_{nlm} c_{jnlm}^{\kappa}(\mathbf{k}) \\ &\quad \times \int d^3r \chi_{k_f}^*(\mathbf{r} - \mathbf{R}' - \mathbf{R}_j' + \mathbf{R} + \mathbf{R}_j) \boldsymbol{\epsilon} \cdot \nabla \Phi_{nlm}(\mathbf{r}) \\ &\approx \frac{1}{V} \sum_{\mathbf{R}} e^{i(\mathbf{k} - \mathbf{k}_f) \cdot \mathbf{R}} \sum_{\mathbf{R}_j} \sum_{nlm} c_{jnlm}^{\kappa}(\mathbf{k}) e^{-i\mathbf{k}_f \cdot \mathbf{R}_j} \\ &\quad \times \int d^3r \chi_{k_f}^*(\mathbf{r}) \boldsymbol{\epsilon} \cdot \nabla \Phi_{nlm}(\mathbf{r}) \\ &= \frac{N}{V} \sum_{\mathbf{G}} \delta_{(\mathbf{k} - \mathbf{k}_f)_{\parallel}, \mathbf{G}} \sum_{\mathbf{R}_j} \sum_{nlm} c_{jnlm}^{\kappa}(\mathbf{k}) e^{-i\mathbf{k}_f \cdot \mathbf{R}_j} \boldsymbol{\epsilon} \cdot \mathbf{M}_{nlm}(\mathbf{k}_f) \\ &= \frac{1}{V_0} \sum_{\mathbf{G}} \delta_{(\mathbf{k} - \mathbf{k}_f)_{\parallel}, \mathbf{G}} \boldsymbol{\epsilon} \cdot \mathcal{M} \cdot \mathbf{c} \\ &\approx \frac{\delta_{\mathbf{k}, \mathbf{k}_f \parallel}}{V_0} \boldsymbol{\epsilon} \cdot \mathcal{M} \cdot \mathbf{c}, \end{aligned} \quad (\text{F10})$$

where  $\mathcal{M}$  is a  $3 \times \dim(\mathbf{c})$  matrix that couples the polarization (row) vector  $\boldsymbol{\epsilon}$  of the incoming light to the initial state (column) vector  $\mathbf{c}(\mathbf{k}) = (\dots, c_{jnlm}^{\kappa}(\mathbf{k}), \dots)^{\top}$ , and where the indices  $\{jnlm\}$  run over all available coordinates and quantum numbers. From the second to the third lines of Eq. (F10), a coordinate transformation  $\mathbf{r} - \mathbf{R} - \mathbf{R}_j \rightarrow \mathbf{r}$  was carried out. Also, from the third to the fourth lines we excluded transitions

between initial-state orbitals at one site  $\Phi_{nlm}(\mathbf{r} - \mathbf{R} - \mathbf{R}_j)$  and final-state waves  $\chi_{k_f}(\mathbf{r} - \mathbf{R}' - \mathbf{R}_j')$  emerging from another site, i.e., we assumed  $\mathbf{R} = \mathbf{R}'$  and  $\mathbf{R}_j = \mathbf{R}_j'$ . This amounts to an explicit exclusion of inter-site final-state scattering (see below) and is commonly referred to as the *independent-center approximation*. From the fourth to the fifth lines, we further identified the Fourier series in  $\mathbf{R}$  as Dirac comb with 2D reciprocal lattice periodicity  $\mathbf{G}$ , and hence recover momentum conservation. Here  $N$  is the number of unit cells in the sample volume and  $V_0$  the unit cell volume.

The column 3-vectors  $\mathbf{M}_{nlm}(\mathbf{k}_f)$  in Eq. (F10) are defined as

$$\mathbf{M}_{nlm}(\mathbf{k}_f) \equiv \int d^3r \chi_{k_f}^*(\mathbf{r}) \nabla \Phi_{nlm}(\mathbf{r}), \quad (\text{F11})$$

where the gradient of atomic orbitals is given in Ref. [48] by

$$\begin{aligned} \nabla \Phi_{nlm}(\mathbf{r}) &= \nabla [R_{nl}(r) Y_l^m(\Omega_r)] \\ &= -\sqrt{\frac{l+1}{2l+1}} \left( \frac{\partial}{\partial r} - \frac{l}{r} \right) R_{nl}(r) Y_{l,l+1,m}(\Omega_r) \\ &\quad + \sqrt{\frac{l}{2l+1}} \left( \frac{\partial}{\partial r} + \frac{l+1}{r} \right) R_{nl}(r) Y_{l,l-1,m}(\Omega_r), \end{aligned} \quad (\text{F12})$$

and where  $Y_{J,L,M}(\Omega_r)$  are the vector spherical harmonics defined as [48]

$$Y_{J,L,M}(\Omega_r) = \sum_{m=-L}^L \sum_{m'=-1}^1 \langle L, m; 1, m' | J, M \rangle Y_L^m(\Omega_r) \boldsymbol{\epsilon}_{m'}, \quad (\text{F13})$$

with Clebsch-Gordon coefficients  $\langle j_1, m_1; j_2, m_2 | J, M \rangle$ .  $Y_{J,L,M}$  thus emerges from the angular-momentum coupling of the ordinary spherical harmonic  $Y_L^m$  with angular momentum quantum number  $L$  to the complex vector  $\mathbf{u} = x\mathbf{e}_x + y\mathbf{e}_y + z\mathbf{e}_z$ ,  $(x, y, z) \in \mathbb{C}^3$ , which has the angular momentum quantum number 1. The eigenstates of the  $\hat{L}_z$  operator in the three-dimensional complex space of  $\mathbf{u}$  are the  $\boldsymbol{\epsilon}_{m'}$ , given by  $\boldsymbol{\epsilon}_{\pm 1} = (-1/\sqrt{2}, -i/\sqrt{2}, 0)^{\top}$ ,  $\boldsymbol{\epsilon}_0 = (0, 0, 1)^{\top}$ , and  $\boldsymbol{\epsilon}_{-1} = (1/\sqrt{2}, -i/\sqrt{2}, 0)^{\top}$  [48]. Defining

$$\begin{aligned} f_{nl}(r) &\equiv \left( \frac{\partial}{\partial r} - \frac{l}{r} \right) R_{nl}(r), \\ g_{nl}(r) &\equiv \left( \frac{\partial}{\partial r} + \frac{l+1}{r} \right) R_{nl}(r), \end{aligned} \quad (\text{F14})$$

we obtain

$$\begin{aligned} \nabla \Phi_{nlm}(\mathbf{r}) &= -\sqrt{\frac{l+1}{2l+1}} f_{nl}(r) Y_{l,l+1,m}(\Omega_r) \\ &\quad + \sqrt{\frac{l}{2l+1}} g_{nl}(r) Y_{l,l-1,m}(\Omega_r), \end{aligned} \quad (\text{F15})$$

which, if inserted into Eq. (F11), yields

$$\begin{aligned} \mathbf{M}_{nlm}(\mathbf{k}_f) &= \int d^3r \chi_{k_f}^*(\mathbf{r}) \left( -\sqrt{\frac{l+1}{2l+1}} f_{nl}(r) Y_{l,l+1,m}(\Omega_r) + \sqrt{\frac{l}{2l+1}} g_{nl}(r) Y_{l,l-1,m}(\Omega_r) \right) \\ &= -\sqrt{\frac{l+1}{2l+1}} e^{-i\sigma_l+1} \tilde{f}_{n,l,l+1}(k_f) Y_{l,l+1,m}(\Omega_{k_f}) + \sqrt{\frac{l}{2l+1}} e^{-i\sigma_l-1} \tilde{g}_{n,l,l-1}(k_f) Y_{l,l-1,m}(\Omega_{k_f}), \end{aligned} \quad (\text{F16})$$

where we exploited the orthogonality of spherical harmonics to resolve the spatial integral and introduced

$$\begin{aligned}\tilde{f}_{n,l,l+1}(k_f) &\equiv 4\pi(-i)^{l+1} \int dr r^2 R_{nl+1}^*(r) f_{nl}(r), \\ \tilde{g}_{n,l,l-1}(k_f) &\equiv 4\pi(-i)^{l-1} \int dr r^2 R_{nl-1}^*(r) g_{nl}(r).\end{aligned}\quad (\text{F17})$$

The two summands in Eq. (F16) correspond to the two dipole-allowed photoemission channels  $l \rightarrow l \pm 1$ . The  $\tilde{f}_{n,l,l+1}(k_f)$  and  $\tilde{g}_{n,l,l-1}(k_f)$  are the kinetic-energy-dependent (through  $k_f$ ) amplitudes of the photoemission  $l + 1$  and  $l - 1$  channels, respectively, for photoemission from an initial state with quantum numbers  $\{nlm\}$ . The  $\sigma_{l+1}$  and  $\sigma_{l-1}$  are their corresponding Coulomb phases.

## 2. Photoemission from C $2p_z$ orbitals without nearest-neighbor scattering

We now focus on photoemission from the  $\pi$  band of graphene and calculate  $M_{k_f k}^\pm$  for this explicit case. Then the matrix  $\mathcal{M}$  is a  $3 \times 2$  matrix, and  $\mathbf{c}$  is given by  $\mathbf{c}^\pm = \frac{1}{\sqrt{2}}(1, \pm e^{i\vartheta_k})^\top$ . Since the orbitals in the two sublattices are identical, the two columns of  $\mathcal{M}$  are also identical. Because a specific choice of the basis in  $\mathbb{C}^3$  is implicit in the definition of the vector spherical harmonics, and thus also in  $\mathbf{M}_{nlm}$ , we also need to express both the polarization vector  $\boldsymbol{\epsilon}$  of the light and the initial state vector  $\mathbf{c}$  in this basis. Since the  $\pi$  bands of graphene involve only C  $2p_z$  states, this is trivial with regard to  $\mathbf{c}$ ; we consider only the  $\mathbf{M}_{210}$  vector. Regarding the polarization vector of the incoming light, we have to choose the basis of eigenstates of the complex vector  $\mathbf{u}$ , i.e.,  $\boldsymbol{\epsilon}_+$ ,  $\boldsymbol{\epsilon}_0$  and  $\boldsymbol{\epsilon}_-$  as defined above. In fact, this basis coincides with circular polarized light of two opposite directions in the  $x, y$  plane ( $\boldsymbol{\epsilon}_+ \equiv \boldsymbol{\epsilon}_\odot$  and  $\boldsymbol{\epsilon}_- \equiv \boldsymbol{\epsilon}_\ominus$ ) and linearly polarized light in the  $z$  direction ( $\boldsymbol{\epsilon}_0$ ).

Applying Eq. (F16) to the C  $2p_z$  orbital with quantum numbers  $\{nlm\} = \{210\}$ , we find

$$\begin{aligned}\mathbf{M}_{210}(\mathbf{k}_f) &= -\sqrt{\frac{2}{3}}e^{-i\sigma_2}\tilde{f}_{2,1,2}(k_f)\mathbf{Y}_{1,2,0}(\Omega_{\mathbf{k}_f}) + \sqrt{\frac{1}{3}}e^{-i\sigma_0}\tilde{g}_{2,1,0}(k_f)\mathbf{Y}_{1,0,0}(\Omega_{\mathbf{k}_f}) \\ &\equiv -\tilde{f}(k_f)\mathbf{Y}_{1,2,0}(\Omega_{\mathbf{k}_f}) + \tilde{g}(k_f)\mathbf{Y}_{1,0,0}(\Omega_{\mathbf{k}_f}),\end{aligned}\quad (\text{F18})$$

where for clarity we absorbed the constants as well as the  $k_f$ -dependent amplitudes ( $\tilde{g}_{2,1,0}$  and  $\tilde{f}_{2,1,2}$ ) and phases ( $e^{-i\sigma_2}$  and  $e^{-i\sigma_0}$ ) in the complex functions  $\tilde{f}(k_f)$  and  $\tilde{g}(k_f)$ , respectively. According to Eq. (F10),  $M_{k_f k}^\pm$  then becomes

$$\begin{aligned}M_{k_f k}^\pm &= \delta_{k,k_{f\parallel}} \boldsymbol{\epsilon} \cdot \mathcal{M}(\mathbf{k}_f) \cdot \mathbf{c}^\pm \\ &= \delta_{k,k_{f\parallel}} (\boldsymbol{\epsilon}_+ \quad \boldsymbol{\epsilon}_0 \quad \boldsymbol{\epsilon}_-) \cdot (\mathbf{M}_{210}(\mathbf{k}_f) \quad \mathbf{M}_{210}(\mathbf{k}_f)) \cdot \frac{1}{\sqrt{2}} \begin{pmatrix} 1 \\ \pm e^{i\vartheta_k} \end{pmatrix} \\ &= \delta_{k,k_{f\parallel}} (\boldsymbol{\epsilon}_+ \quad \boldsymbol{\epsilon}_0 \quad \boldsymbol{\epsilon}_-) \cdot \mathbf{M}_{210}(\mathbf{k}_f) \cdot (1 \quad 1) \cdot \begin{pmatrix} 1 \\ \pm e^{i\vartheta_k} \end{pmatrix} \\ &= \left( \underbrace{-\tilde{f}(k_f) \left[ \sqrt{\frac{3}{10}}\boldsymbol{\epsilon}_- Y_2^1(\Omega_{\mathbf{k}_f}) - \sqrt{\frac{2}{5}}\boldsymbol{\epsilon}_0 Y_2^0(\Omega_{\mathbf{k}_f}) + \sqrt{\frac{3}{10}}\boldsymbol{\epsilon}_+ Y_2^{-1}(\Omega_{\mathbf{k}_f}) \right]}_{d \text{ channel}} + \underbrace{\tilde{g}(k_f)\boldsymbol{\epsilon}_0 Y_0^0(\Omega_{\mathbf{k}_f})}_{s \text{ channel}} \right) \times \frac{1}{\sqrt{2}}(1 \pm e^{i\vartheta_{k_{f\parallel}}}),\end{aligned}\quad (\text{F19})$$

where we used the vector spherical harmonics  $\mathbf{Y}_{1,2,0}(\Omega_{\mathbf{k}_f}) = (\sqrt{\frac{3}{10}}Y_2^{-1}(\Omega_{\mathbf{k}_f}), -\sqrt{\frac{2}{5}}Y_2^0(\Omega_{\mathbf{k}_f}), \sqrt{\frac{3}{10}}Y_2^1(\Omega_{\mathbf{k}_f}))^\top$  and  $\mathbf{Y}_{1,0,0}(\Omega_{\mathbf{k}_f}) = (0, Y_0^0(\Omega_{\mathbf{k}_f}), 0)^\top$  according to Eq. (F13).

First, we note that circular dichroism in this approximation vanishes as  $|Y_2^1(\Omega_{\mathbf{k}_f})| = |Y_2^{-1}(\Omega_{\mathbf{k}_f})|$ . Next, we consider the two experimental geometries NI and OI that are employed in our work. For NI and a vector potential along  $\boldsymbol{\epsilon}_x$ , we have  $\boldsymbol{\epsilon}_+ = -\frac{1}{\sqrt{2}}$ ,  $\boldsymbol{\epsilon}_- = \frac{1}{\sqrt{2}}$ , and  $\boldsymbol{\epsilon}_0 = 0$ . Using the explicit expressions for the spherical harmonics  $Y_0^0(\Omega_{\mathbf{k}_f}) = \frac{1}{2\sqrt{\pi}}$ ,  $Y_2^0(\Omega_{\mathbf{k}_f}) = \sqrt{\frac{5}{4\pi}}(\frac{3}{2}\cos^2\theta - \frac{1}{2})$ ,  $Y_2^1(\Omega_{\mathbf{k}_f}) = -\sqrt{\frac{15}{8\pi}}\sin\theta\cos\theta e^{+i\phi}$ , and  $Y_l^{-m} = (-1)^m Y_l^{m*}$ , Eq. (F19) then becomes

$$M_{k_f k, \text{NI}}^\pm = \delta_{k,k_{f\parallel}} \frac{3}{8\sqrt{\pi}} \tilde{f}(k_f) \sin 2\theta \cos \phi (1 \pm e^{i\vartheta_k}),\quad (\text{F20})$$

and the corresponding photoemission intensity reads

$$I^\pm(k_f, \theta, \phi; h\nu, \epsilon_{\text{NI}}) \propto |M_{k_f k, \text{NI}}^\pm|^2 = \delta_{k, k_{f\parallel}} \frac{9}{64\pi} |\tilde{f}(k_f)|^2 \sin^2 2\theta \cos^2 \phi |1 \pm e^{i\vartheta_k}|^2. \quad (\text{F21})$$

This expression corresponds to Eq. (4). Thus, we find that in the NI geometry with the polarization vector in the surface plane, the photoemission is strictly suppressed in the  $s$  channel. This geometry can therefore be used to determine the (square) modulus of the complex, kinetic-energy-dependent photoemission amplitude in the  $d$  channel.

In the OI geometry, with  $45^\circ$  angle of light incidence in the  $-x, z$  half plane, we have  $(\epsilon_+, \epsilon_0, \epsilon_-) = (-\frac{1}{2}, \frac{1}{\sqrt{2}}, \frac{1}{2})$ . Equation (F19) then yields

$$M_{k_f k, \text{OI}}^\pm = \delta_{k, k_{f\parallel}} \frac{1}{8\sqrt{2\pi}} [\tilde{f}(k_f) (3 \sin 2\theta \cos \phi + 3 \cos 2\theta + 1) + 2\sqrt{2}\tilde{g}(k_f)] \times (1 \pm e^{i\vartheta_k}) \quad (\text{F22})$$

and

$$I^\pm(k_f, \theta, \phi; h\nu, \epsilon_{\text{OI}}) \propto |M_{k_f k, \text{OI}}^\pm|^2 = \delta_{k, k_{f\parallel}} \frac{1}{128\pi} [|\tilde{f}(k_f)|^2 (3 \sin 2\theta \cos \phi + 3 \cos 2\theta + 1)^2 + 8|\tilde{g}(k_f)|^2 + 4\sqrt{2}|\tilde{f}(k_f)||\tilde{g}(k_f)|(3 \sin 2\theta \cos \phi + 3 \cos 2\theta + 1) \cos \Delta\sigma] \times |1 \pm e^{i\vartheta_k}|^2, \quad (\text{F23})$$

which corresponds to Eq. (5), and where  $\Delta\sigma(k_f) \equiv \arg \frac{\tilde{f}(k_f)}{\tilde{g}(k_f)}$  is the kinetic-energy-dependent relative phase between the  $d$  and  $s$  photoemission channels.

### 3. Photoemission from $\pi$ bands of graphene including nearest-neighbor scattering

To account for nearest-neighbor (NN) scattering, we reconsider the matrix element between the full initial- and final-state Bloch functions [Eq. (F10)]:

$$M_{k_f k}^\kappa = \int d^3r \Psi_{k_f}^*(\mathbf{r}) \boldsymbol{\epsilon} \cdot \nabla \Psi_k^\kappa(\mathbf{r}) \\ = \frac{1}{V} \sum_{\mathbf{R}'} e^{-i\mathbf{k}_f \cdot \mathbf{R}'} \sum_{\mathbf{R}'_j} e^{-i\mathbf{k}_f \cdot \mathbf{R}'_j} \sum_{\mathbf{R}} e^{i\mathbf{k} \cdot \mathbf{R}} \sum_{\mathbf{R}_j} \sum_{nlm} c_{jnlm}^\kappa(\mathbf{k}) \int d^3r \chi_{k_f}^*(\mathbf{r} - \mathbf{R}' - \mathbf{R}'_j + \mathbf{R} + \mathbf{R}_j) \boldsymbol{\epsilon} \cdot \nabla \Phi_{nlm}(\mathbf{r}).$$

In the previous section, we assumed  $\mathbf{R}' = \mathbf{R}$  and  $\mathbf{R}'_j = \mathbf{R}_j$  before proceeding with this equation; the initial-state orbital and final-state partial wave were required to be centered on the same carbon atom, i.e., we employed the independent-center approximation. Now we will relax this condition and allow an electron originating from a certain basis atom to be emitted in a partial wave centered on *another* basis atom ( $\mathbf{R}'_j \neq \mathbf{R}_j$ ) in the same unit cell ( $\mathbf{R}' = \mathbf{R}$ ). Clearly, this allows for nearest-neighbor scattering within the unit cell during the photoemission process. Then the above equation becomes

$$M_{k_f k}^\kappa \approx \frac{1}{V} \sum_{\mathbf{R}} e^{i(\mathbf{k} - \mathbf{k}_f) \cdot \mathbf{R}} \sum_{\mathbf{R}'_j} e^{-i\mathbf{k}_f \cdot \mathbf{R}'_j} \sum_{\mathbf{R}_j} \sum_{nlm} c_{jnlm}^\kappa(\mathbf{k}) \int d^3r \chi_{k_f}^*(\mathbf{r} - \mathbf{R}'_j + \mathbf{R}_j) \boldsymbol{\epsilon} \cdot \nabla \Phi_{nlm}(\mathbf{r}) \\ = \frac{1}{V_0} \sum_{\mathbf{G}} \delta_{(\mathbf{k} - \mathbf{k}_f)_\parallel, \mathbf{G}} \sum_{\mathbf{R}'_j} e^{-i\mathbf{k}_f \cdot \mathbf{R}'_j} \sum_{\mathbf{R}_j} \sum_{nlm} c_{jnlm}^\kappa(\mathbf{k}) \int d^3r \chi_{k_f}^*(\mathbf{r} - \mathbf{R}'_j + \mathbf{R}_j) \boldsymbol{\epsilon} \cdot \nabla \Phi_{nlm}(\mathbf{r}). \quad (\text{F24})$$

In the above equation the integral cannot any more be written as  $\boldsymbol{\epsilon} \cdot \mathbf{M}_{nlm}(\mathbf{k}_f)$  for a single set of quantum numbers  $\{nlm\}$  as in Eq. (F16). Rather, the shift  $\boldsymbol{\Delta} = \mathbf{R}_j - \mathbf{R}'_j$  between the centers of the  $\chi_{k_f}$  and  $\Phi_{nlm}$  requires the expansion of the integral in terms of angular momentum eigenfunctions for all quantum numbers  $\{n'l'm'\}$ , with so-called Shibuya-Wulfmann integrals [69,70]  $S_{\mathbf{R},nlm}^{\mathbf{R}'_j, n'l'm'}$  as expansion coefficients,

$$\int d^3r \chi_{k_f}^*(\mathbf{r} - \mathbf{R}'_j + \mathbf{R}_j) \boldsymbol{\epsilon} \cdot \nabla \Phi_{nlm}(\mathbf{r}) = \sum_{n'l'm'} S_{\mathbf{R},nlm}^{\mathbf{R}'_j, n'l'm'} \boldsymbol{\epsilon} \cdot \mathbf{M}_{n'l'm'}(\mathbf{k}_f), \quad (\text{F25})$$

where  $\mathbf{M}_{n'l'm'}$  is given by Eq. (F16). This expansion yields

$$M_{k_f k}^\kappa \approx \frac{1}{V_0} \sum_{\mathbf{G}} \delta_{(\mathbf{k} - \mathbf{k}_f)_\parallel, \mathbf{G}} \sum_{\mathbf{R}'_j} e^{-i\mathbf{k}_f \cdot \mathbf{R}'_j} \sum_{\mathbf{R}_j} \sum_{nlm} c_{jnlm}^\kappa(\mathbf{k}) \sum_{n'l'm'} S_{\mathbf{R},nlm}^{\mathbf{R}'_j, n'l'm'} \boldsymbol{\epsilon} \cdot \mathbf{M}_{n'l'm'}(\mathbf{k}_f) \\ = \frac{1}{V_0} \sum_{\mathbf{G}} \delta_{(\mathbf{k} - \mathbf{k}_f)_\parallel, \mathbf{G}} \sum_{j \in \{\text{A,B}\}} c_j^\pm(\mathbf{k}) \sum_{j' \in \{\text{A,B}\} \forall j' \neq j: i'=0} \sum_{n'l'm'}^2 e^{-i\mathbf{k}_f \cdot \mathbf{n}_{j' i'}} \sum_{n'l'm'} S_{j210}^{j' n'l'm'}(\mathbf{n}_{j' i'}) \boldsymbol{\epsilon} \cdot \mathbf{M}_{n'l'm'}(\mathbf{k}_f), \quad (\text{F26})$$

where in the second line we have adjusted the nomenclature to the case of photoemission from the  $\pi$  bands with band index  $\kappa = \pm$  and quantum numbers  $\{nlm\} = \{210\}$  of graphene with its two sublattices A and B. Note that in the case of graphene (Fig. 5) we have to consider a nonprimitive (larger) unit cell to include all nearest neighbors of the two sublattice atoms into one unit cell. The  $\mathbf{n}_{ji'}$  are the vectors pointing from an atom in sublattice  $j$  to nearest neighbors  $i'$  in the other sublattice. Generally,  $S_{jn'lm}^{jn'l'm'} = \delta_{nm'}\delta_{ll'}\delta_{mm'}$ . Moreover, since both sublattices host the same  $C_3$ -symmetric  $C p_z$  orbitals,  $S_{A210}^{Bn'l'm'} = S_{B210}^{An'l'm'}$  for equivalent  $\mathbf{n}_{ji'}$ . We therefore leave out the sublattice indices  $j, j'$  in the Shibuya-Wulffmann integrals, which according to Eq. (78) in Ref. [70] are proportional to

$$S_{210}^{n'l'm'}(\mathbf{n}_{i'}) \propto \sum_{N,L} \sqrt{6n'N(2l'+1)} \langle l', -m'; 1, 0 | L, -m' \rangle f_{NL}(n_{i'}) Y_L^{-m'}(\boldsymbol{\Omega}_{n_{i'}}). \quad (\text{F27})$$

The Shibuya-Wulffmann integrals perform a basis change between  $C 2p_z$  orbitals centered at sublattice B to a linear combination of orbitals  $\{n'l'm'\}$  centered at sublattice A and vice versa [69,70]. The radial contributions  $f_{NL}$  decay exponentially with orbital distance, i.e.,  $f_{NL} \propto e^{-\frac{Z}{a_0 n'} |\mathbf{n}_{i'}|/2}$  with effective nuclear charge  $Z$  and Bohr radius  $a_0$ , where  $|\mathbf{n}_{i'}|$  in our nearest-neighbor model is equivalent to the sublattice distance  $n_{i'} = 1.421 \text{ \AA}$ , which justifies our nearest-neighbor scattering approximation.

Evaluating Eq. (F26) leads to

$$\begin{aligned} M_{\mathbf{k}_f \mathbf{k}}^\pm &\approx \frac{\delta_{\mathbf{k}, \mathbf{k}_{f\parallel}}}{\sqrt{2}V_0} \boldsymbol{\epsilon} \cdot \left[ (1 \pm e^{i\vartheta_{\mathbf{k}}}) \mathbf{M}_{210}(\mathbf{k}_f) + \sum_{i'=0}^2 \sum_{n'l'm'} \mathbf{M}_{n'l'm'}(\mathbf{k}_f) (S_{210}^{n'l'm'}(\mathbf{n}_{i'}) e^{-i\mathbf{k}_f \cdot \mathbf{n}_{i'}} \pm e^{i\vartheta_{\mathbf{k}}} S_{210}^{n'l'm'}(-\mathbf{n}_{i'}) e^{i\mathbf{k}_f \cdot \mathbf{n}_{i'}}) \right] \\ &= \frac{\delta_{\mathbf{k}, \mathbf{k}_{f\parallel}}}{\sqrt{2}V_0} \boldsymbol{\epsilon} \cdot \left[ (1 \pm e^{i\vartheta_{\mathbf{k}}}) \mathbf{M}_{210}(\mathbf{k}_f) + \sum_{n'l'm'} S_{210}^{n'l'm'}(\mathbf{n}_0) \mathbf{M}_{n'l'm'}(\mathbf{k}_f) \sum_{i'=0}^2 e^{-i\pi \frac{2i'}{3} m'} (e^{-i\mathbf{k}_f \cdot \mathbf{n}_{i'}} \pm e^{i\vartheta_{\mathbf{k}}} e^{-i\pi m'} e^{i\mathbf{k}_f \cdot \mathbf{n}_{i'}}) \right], \quad (\text{F28}) \end{aligned}$$

where we have employed  $c_A^\pm(\mathbf{k}) = \frac{1}{\sqrt{2}}$  and  $c_B^\pm(\mathbf{k}) = \pm \frac{1}{\sqrt{2}} e^{i\vartheta_{\mathbf{k}}}$ . In the second line we have used that the angular components  $Y_L^{-m'}$  in Eq. (F27) transform as  $C_\nu^i Y_L^{-m'} = e^{-i2\pi/\nu m'} Y_L^{-m'}$  under  $\nu$ -fold rotation  $C_\nu$ , thus yielding  $S_{210}^{n'l'm'}(\mathbf{n}_{i'}) = C_3^i S_{210}^{n'l'm'}(\mathbf{n}_0) = e^{-i\pi \frac{2i'}{3} m'} S_{210}^{n'l'm'}(\mathbf{n}_0)$  and  $S_{210}^{n'l'm'}(-\mathbf{n}_0) = C_2 S_{210}^{n'l'm'}(\mathbf{n}_0) = e^{-i\pi m'} S_{210}^{n'l'm'}(\mathbf{n}_0)$ . Further, since the  $2 p_z$  orbital possesses a node in the graphene  $x, y$  plane and the vectors  $\mathbf{n}_{i'}$  connecting the sublattices lie within this plane, the  $S_{210}^{n'l'm'}$  are necessarily zero for  $l' + m' = 0 \pmod 2$ , i.e., for orbitals  $l', m'$  that are nonzero within the  $x, y$  plane.

For electrons to effectively scatter into channels with angular momentum  $l'$ , they further must overcome the centrifugal barrier, i.e.,  $k_f^2 \geq l'(l'+1)/a^2$ , where  $a$  is the atomic radius. With  $a_{\text{carbon}} \sim 0.7 \text{ \AA}$  and  $k_f^{\text{max}} \leq 3 \text{ \AA}^{-1}$  in the energy region where we observe scattering, we find only channels with  $l' < 1.67$  to significantly contribute to this process. The lowest orbital order contributions thus results from  $l' = 1$  and  $m' = 0$ , and we find

$$\begin{aligned} M_{\mathbf{k}_f \mathbf{k}}^\pm &\approx \frac{\delta_{\mathbf{k}, \mathbf{k}_{f\parallel}}}{\sqrt{2}V_0} \boldsymbol{\epsilon} \cdot \left[ (1 \pm e^{i\vartheta_{\mathbf{k}}}) \mathbf{M}_{210}(\mathbf{k}_f) + \sum_{n'} S_{210}^{n'10}(\mathbf{n}_0) \mathbf{M}_{n'10}(\mathbf{k}_f) \sum_{i'=0}^2 (e^{-i\mathbf{k}_f \cdot \mathbf{n}_{i'}} \pm e^{i\vartheta_{\mathbf{k}}} e^{i\mathbf{k}_f \cdot \mathbf{n}_{i'}}) \right] \\ &= \frac{\delta_{\mathbf{k}, \mathbf{k}_{f\parallel}}}{\sqrt{2}V_0} \boldsymbol{\epsilon} \cdot \left[ (1 \pm e^{i\vartheta_{\mathbf{k}}}) \mathbf{M}_{210}(\mathbf{k}_f) + (h^*(\mathbf{k}_{f\parallel}) \pm e^{i\vartheta_{\mathbf{k}}} h(\mathbf{k}_{f\parallel})) \sum_{n'} S_{210}^{n'10}(\mathbf{n}_0) \mathbf{M}_{n'10}(\mathbf{k}_f) \right] \\ &= \frac{\delta_{\mathbf{k}, \mathbf{k}_{f\parallel}}}{\sqrt{2}V_0} \boldsymbol{\epsilon} \cdot \left[ (1 \pm e^{i\vartheta_{\mathbf{k}}}) \mathbf{M}_{210}(\mathbf{k}_f) + (e^{-i\vartheta_{\mathbf{k}_{f\parallel}}} \pm e^{i\vartheta_{\mathbf{k}}} e^{i\vartheta_{\mathbf{k}_{f\parallel}}}) |h^*(\mathbf{k}_{f\parallel})| \sum_{n'} S_{210}^{n'10}(\mathbf{n}_0) \mathbf{M}_{n'10}(\mathbf{k}_f) \right] \\ &= \frac{\delta_{\mathbf{k}, \mathbf{k}_{f\parallel}}}{\sqrt{2}V_0} \boldsymbol{\epsilon} \cdot \mathbf{M}_{210}(\mathbf{k}_f) [(1 \pm e^{i\vartheta_{\mathbf{k}}}) + (e^{-i\vartheta_{\mathbf{k}_{f\parallel}}} \pm e^{i\vartheta_{\mathbf{k}}} e^{i\vartheta_{\mathbf{k}_{f\parallel}}}) u(\mathbf{k}_f)] \\ &= \frac{1}{\sqrt{2}V_0} \underbrace{\boldsymbol{\epsilon} \cdot \mathbf{M}_{210}(\mathbf{k}_f)}_{\text{dipole selection}} \left[ \underbrace{(1 \pm e^{i\vartheta_{\mathbf{k}_{f\parallel}}})}_{\text{horseshoe}} + \underbrace{(e^{-i\vartheta_{\mathbf{k}_{f\parallel}}} \pm e^{i\vartheta_{\mathbf{k}}} e^{i\vartheta_{\mathbf{k}_{f\parallel}}})}_{\text{NN scattering}} u(\mathbf{k}_f) \right]. \quad (\text{F29}) \end{aligned}$$

Here we absorbed the last sum into a complex function  $u(\mathbf{k}_f)$  that essentially describes the overlap between initial-state  $2p_z$  orbitals and scattered Coulomb waves on neighboring sites.  $u(\mathbf{k}_f)$  varies only slowly on the photoemission hemisphere  $\Omega_{\mathbf{k}_f}$  if compared to  $h(\mathbf{k}_f)$  and thus for a given photoelectron momentum  $k_f = \sqrt{2mE_{\text{kin}}/\hbar^2}$  can be approximated as a merely kinetic-energy-dependent fit parameter that is constant across the horseshoe:  $u(\mathbf{k}_f) \sim |u(k_f)| e^{i \arg u(k_f)}$ .

The first term in the square brackets of this expression represents the structure factor producing a photoemission intensity that is proportional to  $|\frac{1}{\sqrt{2}}(1 \pm e^{i\vartheta_{\mathbf{k}}})|^2 = 1 \pm \cos \vartheta_{\mathbf{k}}$  and gives rise to the ubiquitous horseshoe pattern, reflecting the interference of the initial state Bloch wave residing at the graphene sublattices A and B. The second term represents nearest-neighbor scattering in the final state, essentially dictated by  $(e^{-i\vartheta_{\mathbf{k}_{f\parallel}}} \pm e^{i\vartheta_{\mathbf{k}}} e^{i\vartheta_{\mathbf{k}_{f\parallel}}})$ , that reflects the structural

interference between initial *and* final state wave functions. We note that nearest-neighbor final-state scattering now in-

roduces interference terms between  $M_{210}(\mathbf{k}_f)$  and  $M_{n'10}(\mathbf{k}_f)$ , and circular dichroism hence does not vanish any longer.

- 
- [1] S. Hüfner, *Photoelectron Spectroscopy* (Springer, Berlin, 2003).
- [2] A. Damascelli, Probing the electronic structure of complex systems by ARPES, *Phys. Scr.* **T109**, 61 (2004).
- [3] J. A. Sobota, Y. He, and Z.-X. Shen, Angle-resolved photoemission studies of quantum materials, *Rev. Mod. Phys.* **93**, 025006 (2021).
- [4] P. Puschnig, S. Berkebile, A. J. Fleming, G. Koller, K. Emtsev, T. Seyller, J. D. Riley, C. Ambrosch-Draxl, F. P. Netzer, and M. G. Ramsey, Reconstruction of molecular orbital densities from photoemission data, *Science* **326**, 702 (2009).
- [5] S. Moser, An experimentalist's guide to the matrix element in angle resolved photoemission, *J. Electron Spectrosc. Relat. Phenom.* **214**, 29 (2017).
- [6] P. J. Feibelman and D. E. Eastman, Photoemission spectroscopy—Correspondence between quantum theory and experimental phenomenology, *Phys. Rev. B* **10**, 4932 (1974).
- [7] J. W. Gadzuk, Surface molecules and chemisorption. II. Photoemission angular distributions, *Phys. Rev. B* **10**, 5030 (1974).
- [8] P. Woodruff, *Modern Techniques of Surface Science* (Cambridge University Press, Cambridge, 2016).
- [9] P. Puschnig and M. Ramsey, Photoemission tomography: Valence band photoemission as a quantitative method for investigating molecular films, in *Encyclopedia of Interfacial Chemistry*, edited by K. Wandelt (Elsevier, Oxford, 2018), pp. 380–391.
- [10] M. Dauth, T. Körzdörfer, S. Kümmel, J. Ziroff, M. Wiessner, A. Schöll, F. Reinert, M. Arita, and K. Shimada, Orbital Density Reconstruction for Molecules, *Phys. Rev. Lett.* **107**, 193002 (2011).
- [11] P. Puschnig, E.-M. Reinisch, T. Ules, G. Koller, S. Soubatch, M. Ostler, L. Romaner, F. S. Tautz, C. Ambrosch-Draxl, and M. G. Ramsey, Orbital tomography: Deconvoluting photoemission spectra of organic molecules, *Phys. Rev. B* **84**, 235427 (2011).
- [12] D. Lüftner, T. Ules, E. M. Reinisch, G. Koller, S. Soubatch, F. S. Tautz, M. G. Ramsey, and P. Puschnig, Imaging the wave functions of adsorbed molecules, *Proc. Natl. Acad. Sci. USA* **111**, 605 (2014).
- [13] N. L. Nguyen, G. Borghi, A. Ferretti, I. Dabo, and N. Marzari, First-Principles Photoemission Spectroscopy and Orbital Tomography in Molecules from Koopmans-Compliant Functionals, *Phys. Rev. Lett.* **114**, 166405 (2015).
- [14] M. Graus, M. Grimm, C. Metzger, M. Dauth, C. Tusche, J. Kirschner, S. Kümmel, A. Schöll, and F. Reinert, Electron-Vibration Coupling in Molecular Materials: Assignment of Vibronic Modes from Photoelectron Momentum Mapping, *Phys. Rev. Lett.* **116**, 147601 (2016).
- [15] G. Zamborlini, D. Lüftner, Z. Feng, B. Kollmann, P. Puschnig, C. Dri, M. Panighel, G. D. Santo, A. Goldoni, G. Comelli *et al.*, Multi-orbital charge transfer at highly oriented organic/metal interfaces, *Nat. Commun.* **8**, 335 (2017).
- [16] P. Kliuiev, G. Zamborlini, M. Jugovac, Y. Gurdal, K. von Arx, K. Waltar, S. Schnidrig, R. Alberto, M. Iannuzzi, V. Feyrer *et al.*, Combined orbital tomography study of multi-configurational molecular adsorbate systems, *Nat. Commun.* **10**, 5255 (2019).
- [17] R. Wallauer, M. Raths, K. Stallberg, L. Münster, D. Brandstetter, X. Yang, J. Güdde, P. Puschnig, S. Soubatch, C. Kumpf, F. C. Bocquet *et al.*, Tracing orbital images on ultrafast time scales, *Science* **371**, 1056 (2021).
- [18] P. Puschnig and D. Lüftner, Simulation of angle-resolved photoemission spectra by approximating the final state by a plane wave: From graphene to polycyclic aromatic hydrocarbon molecules, *J. Electron Spectrosc. Relat. Phenom.* **200**, 193 (2015).
- [19] J.-H. Park, C. H. Kim, J.-W. Rhim, and J. H. Han, Orbital Rashba effect and its detection by circular dichroism angle-resolved photoemission spectroscopy, *Phys. Rev. B* **85**, 195401 (2012).
- [20] M. Ünzelmann, H. Bentmann, P. Eck, T. Kißlinger, B. Geldiyev, J. Rieger, S. Moser, R. C. Vidal, K. Kißner, L. Hammer *et al.*, Orbital-Driven Rashba Effect in a Binary Honeycomb Monolayer AgTe, *Phys. Rev. Lett.* **124**, 176401 (2020).
- [21] S. Moser, A toy model for dichroism in angle resolved photoemission, *J. Electron Spectrosc. Relat. Phenom.* **262**, 147278 (2023).
- [22] M. Schüler, U. D. Giovannini, H. Hübener, A. Rubio, M. A. Sentef, and P. Werner, Local Berry curvature signatures in dichroic angle-resolved photoelectron spectroscopy from two-dimensional materials, *Sci. Adv.* **6**, eaay2730 (2020).
- [23] M. Schüler, U. De Giovannini, H. Hübener, A. Rubio, M. A. Sentef, T. P. Devereaux, and P. Werner, How Circular Dichroism in Time- and Angle-Resolved Photoemission Can Be Used to Spectroscopically Detect Transient Topological States in Graphene, *Phys. Rev. X* **10**, 041013 (2020).
- [24] M. Schüler, T. Pincelli, S. Dong, T. P. Devereaux, M. Wolf, L. Rettig, R. Ernstorfer, and S. Beaulieu, Polarization-Modulated Angle-Resolved Photoemission Spectroscopy: Toward Circular Dichroism without Circular Photons and Bloch Wave-function Reconstruction, *Phys. Rev. X* **12**, 011019 (2022).
- [25] A. M. Bradshaw and D. P. Woodruff, Molecular orbital tomography for adsorbed molecules: Is a correct description of the final state really unimportant?, *New J. Phys.* **17**, 013033 (2015).
- [26] S. Thevuthasan, G. S. Herman, A. P. Kaduwela, R. S. Saiki, Y. J. Kim, W. Niemczura, M. Burger, and C. S. Fadley, Electron Emission Holography at keV Energies: Estimates of Accuracy and Limitations, *Phys. Rev. Lett.* **67**, 469 (1991).
- [27] P. Krüger, F. Da Pieve, and J. Osterwalder, Real-space multiple scattering method for angle-resolved photoemission and valence-band photoelectron diffraction and its application to Cu(111), *Phys. Rev. B* **83**, 115437 (2011).
- [28] M. Dauth, M. Graus, I. Schelter, M. Wießner, A. Schöll, F. Reinert, and S. Kümmel, Perpendicular Emission, Dichroism, and Energy Dependence in Angle-Resolved Photoemission: The Importance of the Final State, *Phys. Rev. Lett.* **117**, 183001 (2016).
- [29] S. Weiß, D. Lüftner, T. Ules, E. M. Reinisch, H. Kaser, A. Gottwald, M. Richter, S. Soubatch, G. Koller, M. G. Ramsey

- et al.*, Exploring three-dimensional orbital imaging with energy-dependent photoemission tomography, *Nat. Commun.* **6**, 8287 (2015).
- [30] P. Krüger and F. Matsui, Observation and theory of strong circular dichroism in angle-resolved photoemission from graphite, *J. Electron Spectrosc. Relat. Phenom.* **258**, 147219 (2022).
- [31] H. Ebert, D. Ködderitzsch, and J. Minár, Calculating condensed matter properties using the KKR-Green's function method—recent developments and applications, *Rep. Prog. Phys.* **74**, 096501 (2011).
- [32] J. Braun, J. Minár, and H. Ebert, Correlation, temperature and disorder: Recent developments in the one-step description of angle-resolved photoemission, *Phys. Rep.* **740**, 1 (2018).
- [33] S. Beaulieu, J. Schusser, S. Dong, M. Schüler, T. Pincelli, M. Dendzik, J. Maklar, A. Neef, H. Ebert, K. Hricovini *et al.*, Revealing Hidden Orbital Pseudospin Texture with Time-Reversal Dichroism in Photoelectron Angular Distributions, *Phys. Rev. Lett.* **125**, 216404 (2020).
- [34] S. Kera, S. Tanaka, H. Yamane, D. Yoshimura, K. K. Okudaira, K. Seki, and N. Ueno, Quantitative analysis of photoelectron angular distribution of single-domain organic monolayer film: NTCDA on GeS(001), *Chem. Phys.* **325**, 113 (2006).
- [35] N. Komiya, K. Hatada, F. Ota, P. Krüger, T. Fujikawa, and K. Niki, Multiple scattering approach to photoemission from the highest occupied molecular orbital of pentacene, *J. Electron Spectrosc. Relat. Phenom.* **220**, 21 (2017).
- [36] M. Dauth and S. Kümmel, Predicting photoemission intensities and angular distributions with real-time density-functional theory, *Phys. Rev. A* **93**, 022502 (2016).
- [37] U. De Giovannini, H. Hübener, and A. Rubio, A first-principles time-dependent density functional theory framework for spin and time-resolved angular-resolved photoelectron spectroscopy in periodic systems, *J. Chem. Theory Comput.* **13**, 265 (2017).
- [38] C. Riedl, C. Coletti, T. Iwasaki, A. A. Zakharov, and U. Starke, Quasi-Free-Standing Epitaxial Graphene on SiC Obtained by Hydrogen Intercalation, *Phys. Rev. Lett.* **103**, 246804 (2009).
- [39] F. Speck, J. Jobst, F. Fromm, M. Ostler, D. Waldmann, M. Hundhausen, H. B. Weber, and T. Seyller, The quasi-free-standing nature of graphene on H-saturated SiC(0001), *Appl. Phys. Lett.* **99**, 122106 (2011).
- [40] J. Sforzini, L. Nemeč, T. Denig, B. Stadtmüller, T.-L. Lee, C. Kumpf, S. Soubatch, U. Starke, P. Rinke, V. Blum *et al.*, Approaching Truly Freestanding Graphene: The Structure of Hydrogen-Intercalated Graphene on 6H-SiC(0001), *Phys. Rev. Lett.* **114**, 106804 (2015).
- [41] A. Gottwald, H. Kaser, and M. Kolbe, The U125 insertion device beamline at the Metrology Light Source, *J. Synchrotron Radiat.* **26**, 535 (2019).
- [42] A. Bostwick, T. Ohta, T. Seyller, K. Horn, and E. Rotenberg, Quasiparticle dynamics in graphene, *Nat. Phys.* **3**, 36 (2007).
- [43] I. Gierz, J. Henk, H. Höchst, C. R. Ast, and K. Kern, Illuminating the dark corridor in graphene: Polarization dependence of angle-resolved photoemission spectroscopy on graphene, *Phys. Rev. B* **83**, 121408 (2011).
- [44] W. D. Grobman, Angle-resolved photoemission from molecules in the independent-atomic-center approximation, *Phys. Rev. B* **17**, 4573 (1978).
- [45] N. Ueno, K. Suzuki, S. Hasegawa, K. Kamiya, K. Seki, and H. Inokuchi, Angle-resolved photoemission spectroscopy of ultrathin films of H<sub>2</sub>-phthalocyanine on MoS<sub>2</sub> surfaces, *J. Chem. Phys.* **99**, 7169 (1993).
- [46] N. Ueno, A. Kitamura, K. K. Okudaira, T. Miyamae, Y. Harada, S. Hasegawa, H. Ishii, H. Inokuchi, T. Fujikawa, T. Miyazaki, and K. Seki, Angle-resolved ultraviolet photoelectron spectroscopy of thin films of bis(1,2,5-thiadiazolo)-*p*-quinobis(1,3-dithiole) on the MoS<sub>2</sub> surface, *J. Chem. Phys.* **107**, 2079 (1997).
- [47] G. Schönhense, Circular dichroism and spin polarization in photoemission from adsorbates and non-magnetic solids, *Phys. Scr.* **T31**, 255 (1990).
- [48] G. B. Arfken, H. J. Weber, and F. E. Harris, *Mathematical Methods for Physicists*, 7th ed. (Elsevier Academic Press, 2013).
- [49] See Supplemental Material at <http://link.aps.org/supplemental/10.1103/PhysRevResearch.5.033075> for the data plotted in Fig. 3(a); in combination with Eqs. (4) and (5), this data can be used to estimate the photon flux in any photoemission measurement with variable photon energy and geometry based on the photoemission response of a QFMLG sample.
- [50] K. V. Emtsev, F. Speck, T. Seyller, L. Ley, and J. D. Riley, Interaction, growth, and ordering of epitaxial graphene on SiC(0001) surfaces: A comparative photoelectron spectroscopy study, *Phys. Rev. B* **77**, 155303 (2008).
- [51] K. V. Emtsev, A. Bostwick, K. Horn, J. Jobst, G. L. Kellogg, L. Ley, J. L. McChesney, T. Ohta, S. A. Reshanov, J. Röhl *et al.*, Towards wafer-size graphene layers by atmospheric pressure graphitization of silicon carbide, *Nat. Mater.* **8**, 203 (2009).
- [52] S. Forti, K. V. Emtsev, C. Coletti, A. A. Zakharov, C. Riedl, and U. Starke, Large-area homogeneous quasifree standing epitaxial graphene on SiC(0001): Electronic and structural characterization, *Phys. Rev. B* **84**, 125449 (2011).
- [53] L. Broekman, A. Tadich, E. Huwald, J. Riley, R. Leckey, T. Seyller, K. Emtsev, and L. Ley, First results from a second generation toroidal electron spectrometer, *J. Electron Spectrosc. Relat. Phenom.* **144–147**, 1001 (2005).
- [54] C. Bena and G. Montambaux, Remarks on the tight-binding model of graphene, *New J. Phys.* **11**, 095003 (2009).
- [55] M. A. Marques, A. Castro, G. F. Bertsch, and A. Rubio, octopus: A first-principles tool for excited electron–ion dynamics, *Comput. Phys. Commun.* **151**, 60 (2003).
- [56] X. Andrade, J. Alberdi-Rodríguez, D. A. Strubbe, M. J. T. Oliveira, F. Nogueira, A. Castro, J. Muguerza, A. Arruabarrena, S. G. Louie, A. Aspuru-Guzik, A. Rubio, and M. A. L. Marques, Time-dependent density-functional theory in massively parallel computer architectures: The OCTOPUS project, *J. Phys.: Condens. Matter* **24**, 233202 (2012).
- [57] N. Tancogne-Dejean, M. J. T. Oliveira, X. Andrade, H. Appel, C. H. Borca, G. Le Breton, F. Buchholz, A. Castro, S. Corni, A. A. Correa, U. De Giovannini, A. Delgado, F. G. Eich, J. Flick, G. Gil, A. Gomez, N. Helbig, H. Hübener, R. Jestädt, J. Jornet-Somoza *et al.*, Octopus, a computational framework for exploring light-driven phenomena and quantum dynamics in extended and finite systems, *J. Chem. Phys.* **152**, 124119 (2020).
- [58] U. De Giovannini, A. H. Larsen, and A. Rubio, Modeling electron dynamics coupled to continuum states in finite volumes with absorbing boundaries, *Eur. Phys. J. B* **88**, 56 (2015).

- [59] C. Hartwigsen, S. Goedecker, and J. Hutter, Relativistic separable dual-space Gaussian pseudopotentials from H to Rn, *Phys. Rev. B* **58**, 3641 (1998).
- [60] P. A. M. Dirac, Note on exchange phenomena in the Thomas atom, *Math. Proc. Cambridge Philos. Soc.* **26**, 376 (1930).
- [61] J. P. Perdew and A. Zunger, Self-interaction correction to density-functional approximations for many-electron systems, *Phys. Rev. B* **23**, 5048 (1981).
- [62] P. Wopperer, U. De Giovannini, and A. Rubio, Efficient and accurate modeling of electron photoemission in nanostructures with TDDFT, *Eur. Phys. J. B* **90**, 51 (2017).
- [63] N. Mukunda, Completeness of the Coulomb wave functions in quantum mechanics, *Am. J. Phys.* **46**, 910 (1978).
- [64] L. Landau and E. Lifshitz, Schrödinger's equation, in *Quantum Mechanics* (Elsevier, 1977), pp. 50–81.
- [65] M. Abramowitz, I. A. Stegun, and R. H. Romer, Handbook of mathematical functions with formulas, graphs, and mathematical tables, *Am. J. Phys.* **56**, 958 (1988).
- [66] J. Avery and J. Avery, *Generalized Sturmians and Atomic Spectra* (World Scientific, 2006).
- [67] A. Messiah, *Quantum Mechanics* (North-Holland, Amsterdam, 1961).
- [68] J. Humblet, Analytical structure and properties of Coulomb wave functions for real and complex energies, *Ann. Phys.* **155**, 461 (1984).
- [69] V. Aquilanti and A. Caligiana, Sturmian approach to one-electron many-center systems: Integrals and iteration schemes, *Chem. Phys. Lett.* **366**, 157 (2002).
- [70] J. Avery, Many-center Coulomb Sturmians and Shibuya-Wulfman integrals, *Int. J. Quantum Chem.* **100**, 121 (2004).